J. Fluid Mech. (2004), *vol.* 499, *pp.* 75–110.
DOI: 10.1017/S0022112003006931 Printed in the United Kingdom

Large interface deformation in two-layer thermal convection of miscible viscous fluids

By MICHAEL LE BARS AND ANNE DAVAILLE

Laboratoire de Dynamique des Systèmes Géologiques, Institut de Physique du Globe de Paris/CNRS, UMR 7579, 4 Place Jussieu, boite 89, 75 252 Paris cedex 05, France

(Received 4 December 2002 and in revised form 8 August 2003)

Laboratory experiments have been performed to study two-layer thermal convection with large interface deformations. The two fluids have different densities and viscosities but there is neither surface tension nor chemical diffusion at the interface. The initial density stratification is stable, but can be reversed by thermal effects. Two different mechanisms of interface deformation are described: (i) purely thermal features due to convection inside each layer independently can locally and partially deform the interface, leading to dynamic topography; (ii) when the effective buoyancy number (the ratio of the stabilizing chemical density anomaly to the destabilizing thermal density anomaly) reaches a critical value, a whole-layer regime takes place, where the system is fully destabilized and one of the two layers invades the other one in the form of large domes. Several successive pulsations can be observed provided the viscosity ratio is large enough (i.e. > 5). Typical scales (time, length, temperature excess, velocity) and behaviours (direction of spouting, shapes) are determined for each case. Both features are only transient states: because of stirring, the system systematically evolves towards one-layer Rayleigh–Bénard convection. However, this transient state can persist for a very long time compared to the characteristic time scale of thermal convection.

1. Introduction

The interest in two-layer thermal convection has been inspired largely by natural problems, in particular the dynamics of the Earth's mantle (see Tackley 2000 for a recent review); it has also been a theoretical challenge, because of the possibility of Hopf bifurcation and time-dependence at marginal stability (Richter & Johnson 1974). This problem has thus been extensively studied over the past 30 years. However, the simple addion of a second layer considerably complicates the problem of thermal convection and opens up a very large parameter space that has not yet been fully explored.

Stability analysis (Richter & Johnson 1974; Renardy & Joseph 1985; Renardy & Renardy 1985; Le Bars & Davaille 2002) has pointed to the possible occurrence of two different regimes, depending on the buoyancy number B, the ratio of the stabilizing chemical density anomaly to the destabilizing thermal density anomaly: (i) when B is larger than a critical value B_c depending both on viscosity and layer depth ratios, a stratified regime occurs, with convecting patterns developing above and below a stable interface; (ii) when B is lower than the critical value, what we term a 'whole-layer' regime occurs, with a deformed interface and convection patterns developing over the whole depth of the system.

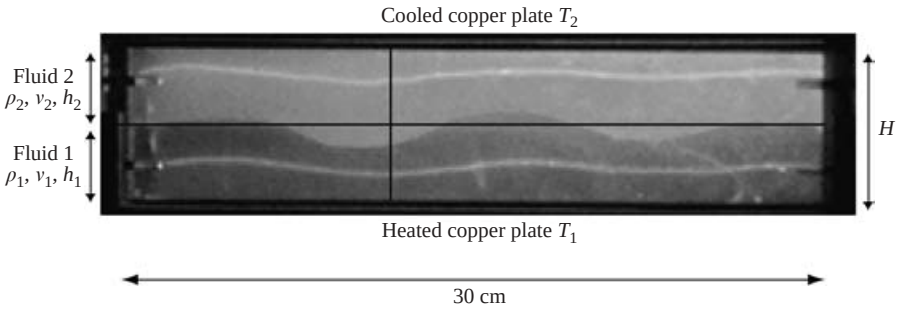

FIGURE 1. Experimental set-up and onset of whole-layer regime in experiment 56 (close to marginal stability). The upper layer 2 is dyed with fluorescein. Vertical and horizontal black lines correspond to the thermocouple probes that measure temperature inside the tank. White lines in the lower and upper layers correspond respectively to isotherms 31 °C and 10 °C (Davaille *et al.* 2003) (in this experiment, $T_2 = 2.5 \pm 0.1$ °C and $T_1 = 38.7 \pm 0.1$ °C). The initial wavelength of interface deformation is equal to twice the tank depth, as predicted by the linear study (Le Bars & Davaille 2002).

Finite-amplitude studies have mostly addressed the stratified case because of its suggested occurrence in the Earth's mantle (Richter & McKenzie 1981; Busse 1981; Olson 1984; Cserepes & Rabinowicz 1985; Ellsworth & Schubert 1988; Cserepes, Rabinowicz & Rosemberg-Borot 1988; Sotin & Parmentier 1989; Cardin, Nataf & Dewost 1991; Olson & Kincaid 1991; Davaille 1999*a*). Other studies have also been performed to characterize the respective influence of thermal and mechanical coupling between layers, but restricting the interface to remain flat (Rasenat, Busse & Rehberg 1989; Busse & Sommermann 1996; Andereck, Colovas & Degen 1996; Degen, Colovas & Andereck 1998). In particular, they describe a time-dependent behaviour, involving no deformation of the interface, with a convective pattern oscillating between viscous and thermal coupling.

Recently, the whole-layer regime has been reported experimentally by Davaille (1999*b*): focusing on the interaction of thermal convection with a sharp discontinuity in density and viscosity in the parameter range likely to be relevant to the Earth's mantle, she observed large periodic interface deformations developing over the whole depth of the system. Using the same experimental set-up (figure 1), Le Bars & Davaille (2002) showed that close to marginal stability, the early scales of the whole-layer regime are predicted well by linear analysis. At large Rayleigh number Ra, the situation is complicated by the superimposition of various types of convective features: in each of the two fluids, the destabilization of its outer thermal boundary layer possibly leads to the formation of small-scale plumes as in classical Rayleigh–Bénard convection (Howard 1964), thus referred to as 'purely thermal'; but purely thermal features from hot and cold plates also interact at the interface, where they induce a large-scale thermochemical regime, either with a stable interface (even if partly deformed), thus corresponding to the stratified regime, or with a fully destabilized interface, thus corresponding to the whole-layer regime. As shown in figure 2, the critical value $B_c(\gamma, a)$ (where γ is the viscosity ratio between the two layers and a their depth ratio) determined by marginal stability – typically ranging between 0.2 and 0.5 – is still relevant for the early stages of experiments (a few overturn times), but the system then evolves over time.

In the present study, we focus on cases where the interface deforms: our purpose is to extend the initial conclusions presented above by precisely describing the onset,

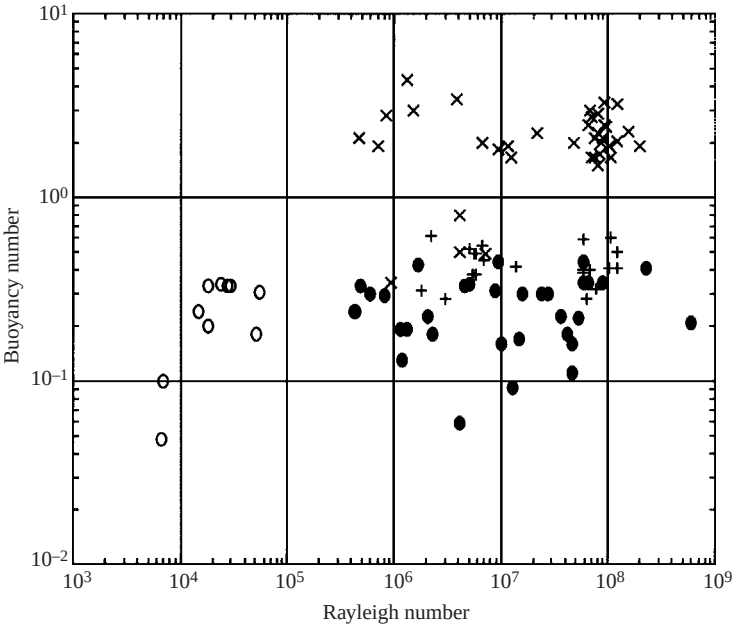

FIGURE 2. Observed initial large-scale thermochemical regime as a function of Rayleigh and buoyancy numbers: ●, × and + represent experiments where the initial large-scale regime is respectively the whole-layer regime, the stratified regime (including points from Davaille 1999*a*, where $B > 1$) and the stratified regime with partly deformed interface. Open circles denote experiments close to marginal stability, where only one scale of convection is excited.

Tank	Length (cm)	Width (cm)	Depth H (cm)	
1	30	30	6.1	
2	30	30	14.8	
3	30	10	16.4	'2D tank'
4	30	30	8.0	

TABLE 1. Dimensions of the four tanks.

patterns and evolution of the various convective features. Experimental conditions are summarized in § 2 and possible behaviours of the whole-layer regime close to marginal stability are presented in § 3. We then address large-Ra dynamics: § 4 focuses on the small-scale purely thermal mode and § 5 on the large-scale whole-layer thermochemical mode. Section 6, finally, characterizes the time-evolution and the progressive stirring of the two fluids.

2. Experimental conditions

The experimental set-up is similar to Davaille (1999*a*) (figure 1): two miscible fluids with different kinematic viscosities (ν_1 and ν_2), densities (ρ_{1_0} and ρ_{2_0} at temperature T_0) and depths (h_1 and h_2), initially at ambient temperature, are superimposed in a tank (see dimensions in table 1). Working fluids are a mixture of water, cellulose ($< 2\%$ in weight) and salt ($< 7\,\mathrm{kg\,m^{-3}}$) (see Tait & Jaupart 1989 and Appendix A), except for experiment 13 where miscible Newtonian silicon oils (Rhodorsil 47V5000

Probe	Coordinate in cm measured from the extremity						
Vertical	0.35	0.60	1.25	2.05	3.90	5.95	7.20
	8.20	9.25	10.25	12.70	13.70	14.30	14.70
Horizontal	7.00	8.00	9.05	9.60	10.15	10.65	12.70
	14.80	15.85	16.30	16.80	18.05	19.05	

TABLE 2. Location of thermocouples in the vertical and horizontal probes (precision of ± 0.03 cm). In all experiments, thermocouples were also located in the bottom and top boundary plates.

and 45*V*500) are used. At time $t = 0$, both baths are turned on, and the lower (upper) copper plate is continuously heated (cooled) until the bath has reached its assigned temperature T_1 (T_2), typically after 10 minutes.

The initial density distribution is stable, and because of experimental constraints, the heaviest fluid 1 is also always the most viscous. The Prandtl number in each layer is always greater than 100 to ensure that inertial effects are non-existent (Krishnamurti 1970). The high viscosities render diffusion of salt across the interface extremely slow compared to the characteristic time scale of the instabilities, so that its effects on mixing are negligible compared to other mechanical entrainment processes (more details can be found in Davaille 1999*a*). Up to 29 thermocouples are used to measure the local temperature at selected points, located in the boundary plates and on a vertical and a horizontal probe (see figure 1 and table 2). All temperatures are read every 30 s through a scanning voltmeter connected to a computer.

Physical properties of both layers are measured for each experiment: the only important uncertainty comes from the viscosity measurements (accuracy of 25%). For natrosol solutions, the viscosities and the coefficient of thermal expansion α are temperature-dependent (see Appendix A): it is thus difficult to choose meaningful values. However, we expect that motions taking place in each layer separately (i.e. purely thermal convection) are mostly driven by boundary layer instabilities: values at the mean temperature of the boundary layer are then used. We also expect that processes taking place over the whole depth of the tank and involving both layers (i.e. thermochemical convection) are mostly driven by instabilities at the interface: values at a reference temperature of 20 °C (i.e. the initial mean temperature of the tank) are used. This is somewhat arbitrary, but note that (i) for most experiments, the temperature-dependence of viscosity is smaller than its composition-dependence, and (ii) according to the linear theory, changes of the thermal expansion coefficient have a minor effect on convection (see Appendix B).

Apart from the Prandtl number, four dimensionless numbers are necessary to fully describe the two-layer system:

the viscosity ratio

$$\gamma = \frac{\nu_1}{\nu_2}; \tag{2.1}$$

the layer depth ratio

$$a = \frac{h_1}{H}, \tag{2.2}$$

where $H = h_1 + h_2$;

the Rayleigh number

$$Ra = \frac{\alpha g \Delta T H^3}{\kappa \nu_2}, \tag{2.3}$$

where κ is the thermal diffusivity coefficient and $\Delta T = T_1 - T_2$ (it is sometimes more convenient to use the Rayleigh number of each layer taken separately

$$Ra_i = \frac{\alpha_i g \Delta T_i h_i^3}{\kappa \nu_i}, \tag{2.4}$$

where ΔT_i is the temperature change through layer i and α_i the thermal expansion coefficient at the mean temperature of layer i);
the buoyancy number, the ratio of stabilizing chemical density anomaly to destabilizing thermal density anomaly

$$B = \frac{\Delta \rho_\chi}{\alpha \rho_0 \Delta T}, \tag{2.5}$$

where $\Delta \rho_\chi = \rho_{1_0} - \rho_{2_0}$ is the chemical stratification and $\rho_0 = (\rho_{1_0} + \rho_{2_0})/2$.

In the above definitions γ and a characterize the mechanical differences between the two layers, Rayleigh numbers measure the strength of convection, and B determines the stability of the whole system and the ability of the interface to deform. Values of the parameters for the 59 experiments are listed in table 3. This set of experiments allows us to separate several different behaviours from the simple trend presented in figure 2: all regimes indexed in table 3 are schematically presented in figure 3 and will be precisely described in the following.

3. Whole-layer regime at low Rayleigh number

Ten experiments were performed close to marginal stability. In our experiments, the two fluids are initially at the same temperature T_0, and then heated from below and cooled from above. Outer thermal boundary layers subsequently grow from the hot and cold plates (phase (i) on figure 4*b*) until a linear temperature profile is established through the whole tank. Then, provided the critical Rayleigh number is reached, convection starts in the form of large domes with a wavelength comparable to twice the tank depth (figure 1), which grow in both directions until they reach the opposite boundary (phase (ii) on figure 4*b*). The wavelength and time scale of these convective features are predicted well by marginal stability analysis (see Le Bars & Davaille 2002). Their subsequent behaviour ranges between two limit cases: overturning and oscillations.

3.1. *Overturning*

In some experiments, for instance experiment 46 presented in figure 4, the domes spread under the boundary plates, cool down (respectively heat up) and finally sink (respectively rise) encapsulating pockets of the other fluid in the process. This corresponds to phase (iii) on figure 4(*b*). The temperature structure then remains fixed throughout the rest of the experiment (phase (iv) on figure 4*b*): the convective motions are steady and the initial heterogeneities are stirred and stretched by the flow. When their size becomes small enough, they are finally completely erased by chemical diffusion.

3.2. *Oscillations*

Very close to Ra_c, thermal effects just compensate chemical stratification, thermal diffusion and viscous dissipation. Then hot domes still develop but they do not

Experiment	γ	a	B	Ra	Behaviour	Tank
1	27	0.5	0.13	1.2×10^6	WL1icr	1
2	12	0.5	0.24	1.5×10^4	WLosc → comp	1
3	12	0.5	0.18	5.2×10^4	WLcomp	1
5	190	0.5	0.33	4.8×10^5	WL1vo	1
6	170	0.25	0.24	4.3×10^5	TD → WL1vo	1
7	150	0.75	0.24	4.2×10^5	WLcomp	1
8	13	0.5	0.16	1.0×10^7	WL1vo	2
9	22	0.25	0.17	1.5×10^7	WL1icr	2
10	100	0.25	0.33	4.6×10^6	TD → WL1vo	2
13	8	0.25	0.093	1.3×10^7	WL1icr	2
16	1	0.25	0.29	8.0×10^5	TD → WL1overturn	2
17	1	0.75	0.3	5.9×10^5	WL2overturn	2
18	21	0.3	0.31	8.8×10^6	WL1vo	2
19	17	0.3	0.55	6.6×10^6	TD	2
20	15	0.3	0.8	4.1×10^6	STR/small TD	2
21	9	0.3	0.49	5.8×10^6	TD	2
22	12	0.3	0.38	5.9×10^6	TD	2
23	100	0.3	0.5	4.1×10^6	STR	2
24	16	0.3	0.46	6.8×10^6	TD	3
25	37	0.3	0.39	5.9×10^7	TD	2
26	590	0.9	0.28	6.3×10^7	TD	2
27	30	0.9	0.11	4.7×10^7	WL2icr	2
28	11	0.6	0.49	7.1×10^6	STR → WL1	2
29	30	0.83	0.4	5.9×10^7	TD	2
30	20	0.83	0.49	5.6×10^6	TD	2
31	25	0.83	0.18	4.2×10^7	WL2icr	2
32	1.7	0.6	0.34	5.1×10^6	strat → WL2overturn	2
33	1.3	0.57	0.43	1.7×10^6	strat → WL2overturn	2
35	77	0.25	0.4	6.8×10^7	TD → WL1vo	2
36	23	0.9	0.59	5.8×10^7	TD	2
37	1.8	0.5	0.28	3.0×10^6	TD → WL1overturn	2
38	70	0.5	0.22	5.4×10^7	WL1vo	2
39	1	0.25	0.62	2.2×10^6	strat → TD	2
40	23	0.75	0.42	1.4×10^7	TD	2
41	1400	0.75	0.32	7.7×10^7	TD	2
42	22	0.75	0.18	2.3×10^6	WL2 or 1 icr	2
43	24	0.69	0.19	1.3×10^6	WL2 or 1 icr	2
44	2	0.69	0.059	4.1×10^6	WL2overturn	2
45	1.3	0.44	0.1	6.8×10^3	WLoverturn	4
46	1.1	0.44	0.048	6.7×10^3	WLoverturn	4
47	6.7	0.5	0.2	1.8×10^4	WLosc	4
48	6.5	0.55	0.34	2.4×10^4	WLcomp	4
49	7	0.55	0.33	2.9×10^4	Wloverturn	4
50	10	0.55	0.3	5.5×10^4	Wloverturn	4
51	4.1	0.5	0.33	1.8×10^4	WLoverturn	4
52	140	0.3	0.3	2.4×10^7	WL1vo	2
53	180	0.5	0.3	2.7×10^7	WL1vo	2
54	190	0.3	0.23	3.6×10^7	WL1vo	2
56	6.8	0.5	0.33	2.8×10^4	WLcomp	4
57	83	0.29	0.38	5.5×10^6	TD → WL1vo	2
58	10	0.75	0.19	1.2×10^6	WL2overturn	2
60	14	0.3	0.53	5.1×10^6	TD	2
61	6.8	0.78	0.31	1.8×10^6	TD	2
62	7.7	0.78	0.23	2.1×10^6	WL2icr	2
63	36	0.83	0.16	4.6×10^7	WL2icr	2

Continued

Experiment	γ	a	B	Ra	Behaviour	Tank
5–98	150	0.41	0.34	9.0×10^7	WL1	2
6–98	46	0.91	0.21	5.9×10^8	WL2	2
7–98	34	0.3	0.3	1.6×10^7	WL1	2
A800	4000	0.51	0.41	2.3×10^8	WL1	2
uncertainty	50%	5%	10%	40%		

TABLE 3. Values of experimental dimensionless numbers (γ, a, B, Ra) and observed thermochemical regime. TD = dynamic topography, STR = stratified, WL = whole-layer; close to marginal stability: osc = oscillations, comp = composite overturn/oscillations; at large Ra: vo = vertical oscillations, icr = initial configuration reversals, 1 = most viscous layer invading, 2 = less viscous layer invading. The tank used is also indicated for each experiment (see table 1).

spread under the cold plate before cooling down (figure 5*a*) and no large-scale stirring occurs. Although the interface is highly deformed, the two fluids remain separate and travelling waves with a period comparable to predictions from marginal stability analysis can be observed for several days (figure 5*b*, *c*). This behaviour is most easily observed when the viscosity contrast is relatively large ($\gamma > 5$ or $\gamma < 1/5$) and/or when the buoyancy ratio is close to critical, in agreement with theoretical linear analysis (see Le Bars & Davaille 2002).

However, oscillations lasting several days are quite difficult to obtain experimentally because they occur in a very narrow (Ra, B) window (Richter & Johnson 1974; Le Bars & Davaille 2002) and are very sensitive to small perturbations in the thermal boundary conditions. Besides, the limited aspect ratio of our tanks (see table 1) probably prevents the setting up of stable structures. Therefore, in most experiments, both overturning and oscillation modes combine and some pulsations are observed before complete mixing. For example, the experiment presented in figure 6 is in the appropriate (Ra, B) range, but exhibits an asymmetric encapsulating structure: in the right half of the tank, overturning patterns comparable to those presented in figure 4 take place; in the left half of the tank, two zones constituted mostly of fluid 1 and fluid 2 respectively are observed. These zones behave like the domes seen in figure 5(*a*), and also travel; but stirring is sufficiently efficient to lead to one-layer convection after three pulsations (figure 6*b*, *c*).

In the following, we will focus on large-Ra dynamics. Then, two types of convective features are superimposed at two different length scales: in each fluid, purely thermal features as shown in figure 7 arise from the destabilization of the outer thermal boundary layers, whereas the large-scale thermochemical mode occurs at the interface from the interaction between the two fluids.

4. Large-Rayleigh-number dynamics: characteristics of the small-scale purely thermal mode

4.1. *Onset of purely thermal convection*

At high Rayleigh numbers, the onset of convection corresponds to the appearance of purely thermal features, coming out of the growing thermal boundary layers either in layer 1 above the hot plate or in layer 2 below the cold plate. The behaviour of each fluid taken separately is comparable to the classical one-fluid Rayleigh–Bénard convection: when the layer Rayleigh number Ra_i is supercritical, the thermal features

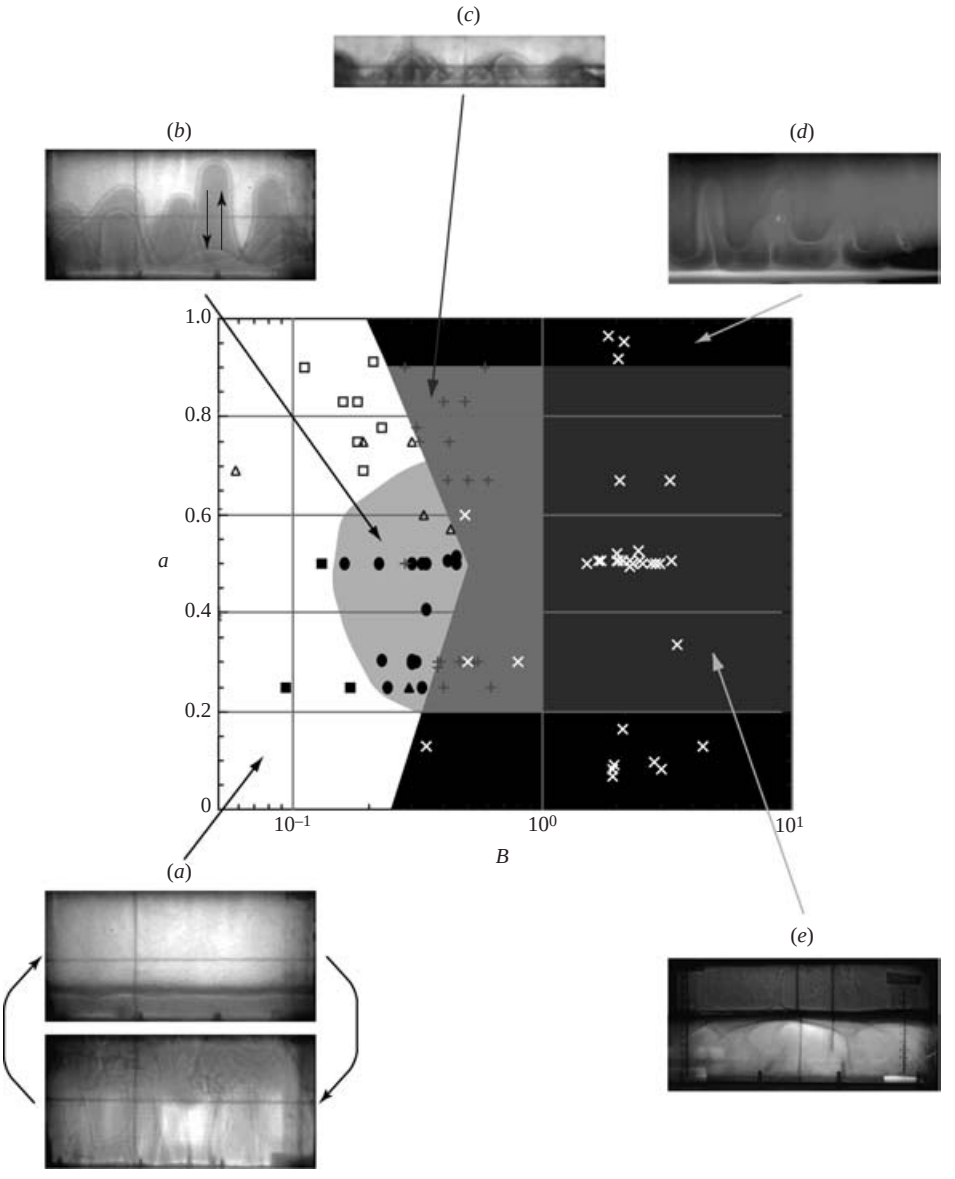

FIGURE 3. Regime diagram as a function of the buoyancy number B and the layer depth ratio a: triangles correspond to immediate mixing, squares to initial configuration reversals illustrated in (a) and circles to vertical oscillations illustrated in (b); open symbols correspond to domes from the upper less viscous fluid 2, and filled symbols to domes from the lower most viscous fluid 1. As in figure 2, + represents stratified experiments with interface deformations as in (c), which possibly evolve towards destabilization, and × stratified regime with a flat interface (including points from Davaille 1999*a*, where $B > 1$): thermochemical plumes shown in (d) occur when one layer is thinner than the corresponding thermal boundary layer (see Davaille, Girard & Le Bars 2002); when both layers are large enough, convection develops above and below the interface as in (e).

inside fluid i take the form either of cells with a typical size comparable to the layer depth or of plumes arising from the destabilization of the corresponding outer thermal boundary layer (figure 7). For $Ra_i > 10^4$, typically, the onset time scales as

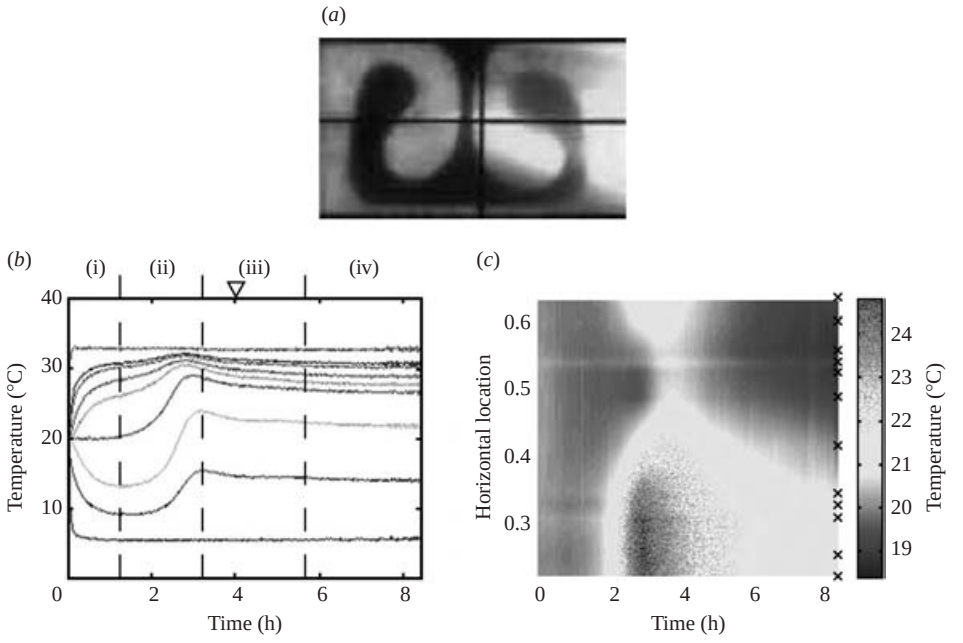

FIGURE 4. (*a*) Picture, (*b*) temperature signal measured by the vertical thermocouple probe and (*c*) horizontal temperature measured by the horizontal thermocouple probe for experiment 46, where overturning occurs. On (*b*) the triangle shows the time when the picture was taken; successive curves at decreasing temperatures correspond to thermocouples located at 0, 0.35, 0.60, 1.25, 2.05, 3.90, 5.95, 7.20 and 8 cm from the hot lower plate. Phase (i) corresponds to the establishment of a linear temperature profile by conduction from the copper plates, phase (ii) to a rising hot dome, phase (iii) to the cooling of this dome and phase (iv) to the steady state. On (*c*), the horizontal location is normalized by the width of the tank; crosses on the right show the location of the thermocouples.

(Howard 1964)

$$\tau_i = \frac{h_i^2}{\pi\kappa}\left(\frac{Ra_c}{Ra_i}\right)^{2/3}. \tag{4.1}$$

Our measurements follow this model well (figure 8): the best fit to a $Ra_i^{-2/3}$ law gives a critical Rayleigh number $Ra_c = 1300 \pm 500$, in agreement with the value of 1641 ± 422 determined experimentally by Davaille (1999*a*) (in this reference, the coefficient π was omitted in the theoretical expression (3) p. 230 but was taken into account for the calculations). Since, during the onset of convection, the copper plate temperature conditions were somewhere between 'fixed flux' and 'constant temperature', these experimental results should be compared to the following theoretical values: (i) $Ra_c = 1100.7$ for a shear-stress-free isothermal upper boundary and a rigid isothermal lower boundary (Pellew & Southwell 1940), and (ii) $Ra_c = 816.7$ for a shear-stress-free isothermal upper boundary and a heat-flux-prescribed rigid lower boundary (Sparrow, Goldstein & Jonsson 1964). Taking into account uncertainties in our measurements, theoretical and experimental values show reasonable agreement.

4.2. *Interaction with the interface: dynamic topography*

When thermal plumes reach the interface, they are affected by both density and viscosity contrasts. For large buoyancy ratio ($B > 1$ typically), the chemical stratification acts like a barrier and prevents penetration. However, when $B \leqslant 1$,

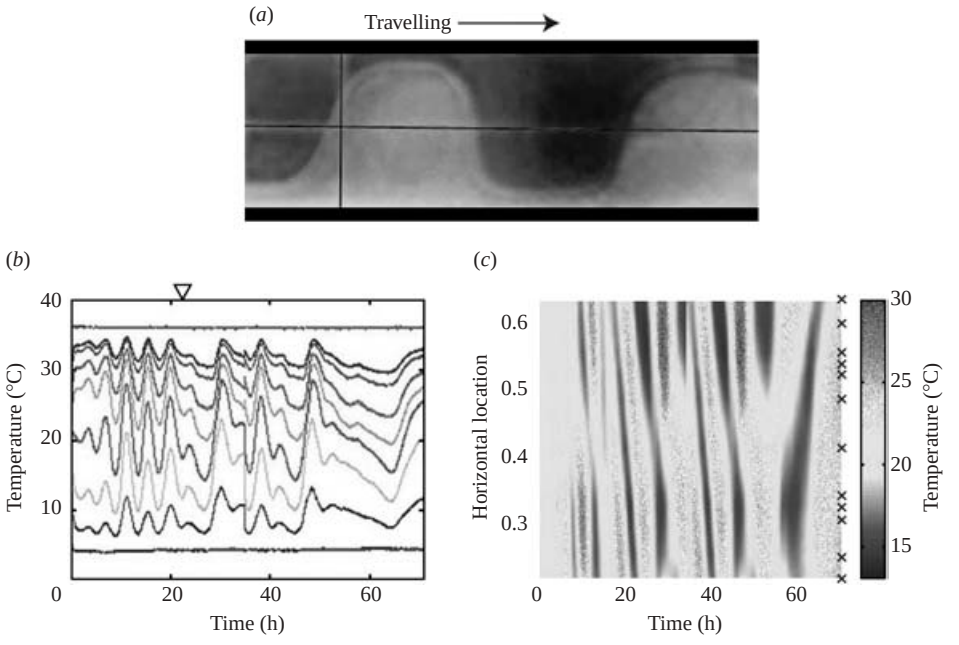

FIGURE 5. As figure 4 but for experiment 47, where travelling waves are recorded over several days.

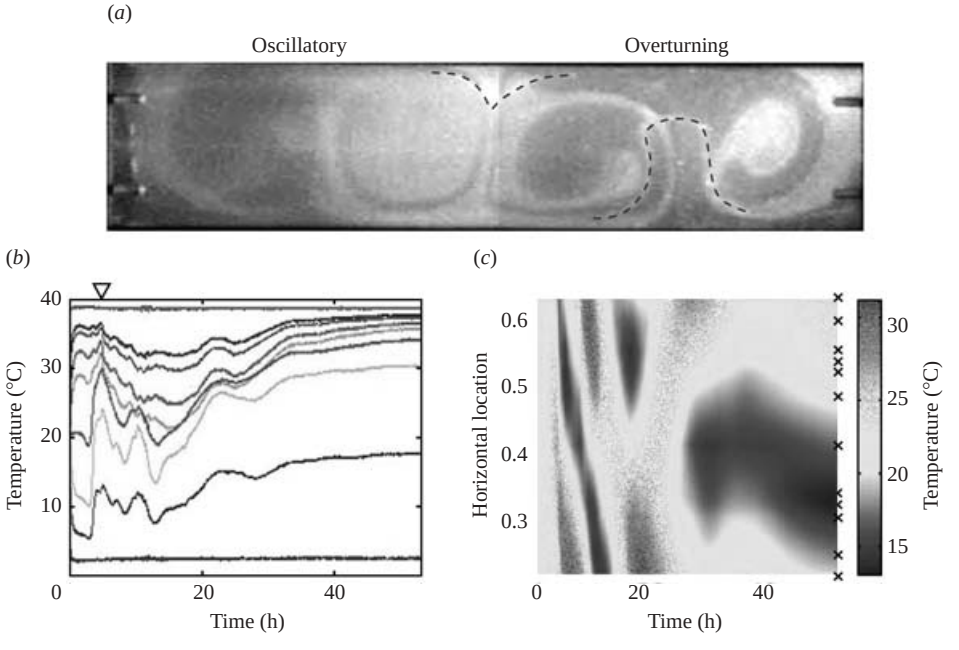

FIGURE 6. As figure 4 but for experiment 56, where three oscillations are recorded before overturning (dashed lines show isotherms 31 °C and 10 °C for outer boundary temperatures of 2.5 ± 0.1 °C and 38.7 ± 0.1 °C, Davaille *et al.* 2003).

thermal features from one of the outer boundaries can partly and locally destabilize the interface. We call this 'dynamic topography', because it is essentially due to motions in each of the layers taken separately.

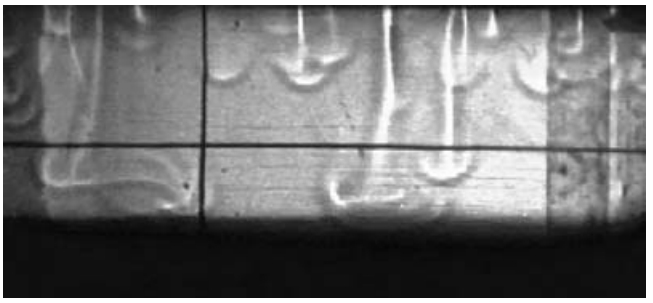

FIGURE 7. Purely thermal plumes in layer 2 arising from the destabilization of the cold thermal boundary layer (experiment 13).

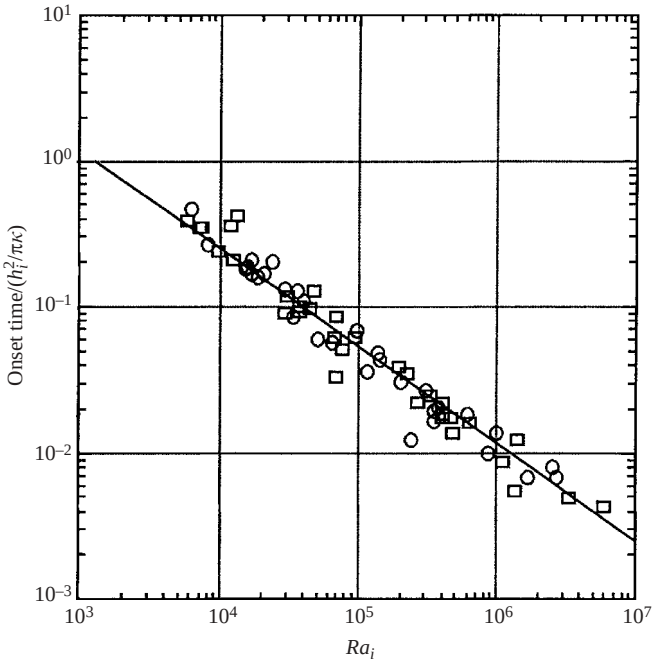

FIGURE 8. Thermal onset times in layer 1 (circles) and layer 2 (squares) as a function of the layer Rayleigh number. The onset is defined as the time at which the temperature in the boundary layer deviates from the initial conductive trend: with this method, the critical time for the onset of convective instabilities is determined with an error of ± 15 s, i.e. between two successive temperature scans. When possible, this measurement was confirmed with direct observation of the appearance of thermal plumes. The line corresponds to the best fit according to (4.1): the experimental critical value is $Ra_c = 1300 \pm 500$.

4.2.1. *Thermal plumes from the most viscous layer*

This is the most likely case to generate topography at the interface, since the only barrier to interface deformation is the density stratification. Then, once convection has started in the most viscous layer, fluid 1 can locally penetrate fluid 2. It does so in the form of cylinders with an almost constant diameter comparable to the thermal boundary layer thickness δ_1 (figure 9); however the whole system remains stable. These instabilities stop before reaching the opposite boundary.

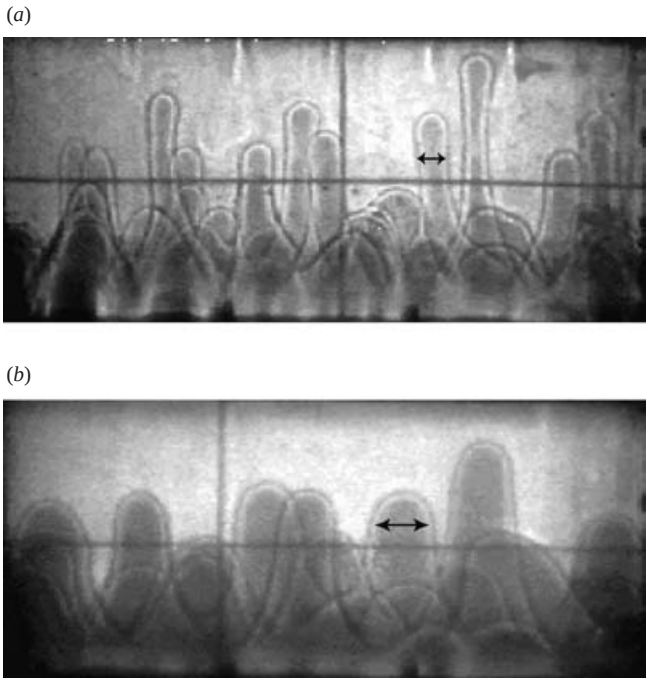

FIGURE 9. Pictures of dynamic topography due to the most viscous layer 1. (*a*) Experiment 25: the arrow shows the measured typical diameter (1.4 ± 0.1 cm), which is close to the thermal boundary layer thickness $\delta_1 = 1.5 \pm 0.1$ cm measured by the vertical thermocouple probe. (*b*) Experiment 22: the arrow shows the measured typical diameter (2.5 ± 0.2 cm), close to the thermal boundary layer thickness $\delta_1 = 2.3 \pm 0.1$ cm measured by the vertical thermocouple probe.

From the equations of motion, this behaviour can be modelled simply by adding a stratification term (due to the chemical density contrast) to the classical equations for Rayleigh–Bénard convection (see for instance Turner 1979, pp. 208–209). In our experiments, inertial effects are negligible: motions are thus controlled by the equilibrium between buoyancy effects and viscous drag forces. Let θ and w be the typical temperature excess and the typical convective velocity. When a thermal plume from layer 1 rises into fluid 2, its buoyancy is reduced because of the chemical stratification $\Delta\rho_\chi$, while viscous drag forces remain dominated by motions in the most viscous fluid 1 (Whitehead & Luther 1975). Hence, at first order, the equation of motion becomes

$$\eta_1 \frac{w}{\delta_1^2} \sim (\alpha\rho\theta - \Delta\rho_\chi)g. \tag{4.2}$$

Because of heat diffusion, the temperature excess evolves through time: the scaling linear analysis gives

$$\frac{\partial\theta}{\partial t} \sim -\kappa \frac{\theta}{\delta_1^2}, \tag{4.3}$$

thus

$$\theta \sim \Delta T \exp(-t/\tau), \tag{4.4}$$

where $\tau = \delta_1^2/\kappa$ is the typical time of diffusion through a plume. The motion of a diapir of fluid 1 into fluid 2 therefore is given by

$$\eta_1 \frac{w}{\delta_1^2} \sim (\alpha\rho\Delta T \exp(-t/\tau) - \Delta\rho_\chi)g. \tag{4.5}$$

According to this equation, dynamic topography is possible only if $\alpha\rho\Delta T > \Delta\rho_\chi$, which means $B < 1$: the velocity then vanishes at time

$$t_{max} \sim -\tau \ln(B), \tag{4.6}$$

which also gives the maximum elevation.

Let $p(t)$ be the penetration of fluid 1 above the interface: to first order, we can write

$$\frac{\mathrm{d}p}{\mathrm{d}t} \sim w. \tag{4.7}$$

Integration in time of (4.7) using (4.5) leads to

$$p(t) \sim \frac{\alpha\rho g\Delta T\delta_1^4}{\kappa\eta_1}(1 - \exp(-t/\tau)) - \frac{\Delta\rho_\chi g\delta_1^4}{\kappa\eta_1}\frac{t}{\tau}, \tag{4.8}$$

taking $p(0) = 0$. This can also be written

$$p(t) = C_1\frac{\alpha\rho g\Delta T\delta_1^4}{\kappa\eta_1}\left(1 - \exp(-t/\tau) - B\frac{t}{\tau}\right), \tag{4.9}$$

where C_1 is a scaling factor which will be determined experimentally. We see that the interface initially rises because of the thermal buoyancy, but it finally sinks because of the combined effects of thermal diffusion and chemical stratification. The maximum height is given by

$$p(t_{max}) = C_1\frac{\alpha\rho g\Delta T\delta_1^4}{\kappa\eta_1}(1 - B + B\ln(B)), \tag{4.10}$$

provided $p(t_{max})$ remains lower than the layer 2 depth. Scaling laws (4.9) and (4.10) explain the data well (figures 10 and 11), provided that the experimental constant is $C_1 = 0.0031 \pm 0.0011$. Also, the time for maximum elevation in figure 10 is

$$t_{max} = -(0.058 \pm 0.006)\tau \ln(B), \tag{4.11}$$

introducing a scaling factor $C_2 = 0.058 \pm 0.006$ in (4.6). Numerical values of C_1 and C_2 are both consistent with choosing a characteristic length scale $\widetilde{\delta_1} = (0.24 \pm 0.08)\delta_1$ instead of δ_1: this may be linked to the cylindrical morphology of the structures studied.

4.2.2. *Thermal plumes from the less viscous layer*

This configuration is less favourable to partial invasion since a thermal plume coming from the less viscous layer 2 encounters a viscosity increase as well as a density stratification at the interface. Therefore, it will deform the interface only if the most viscous layer is stagnant: interface topography is then moulded progressively by several successive thermal plumes on a much longer time scale than in the previous case (figure 12).

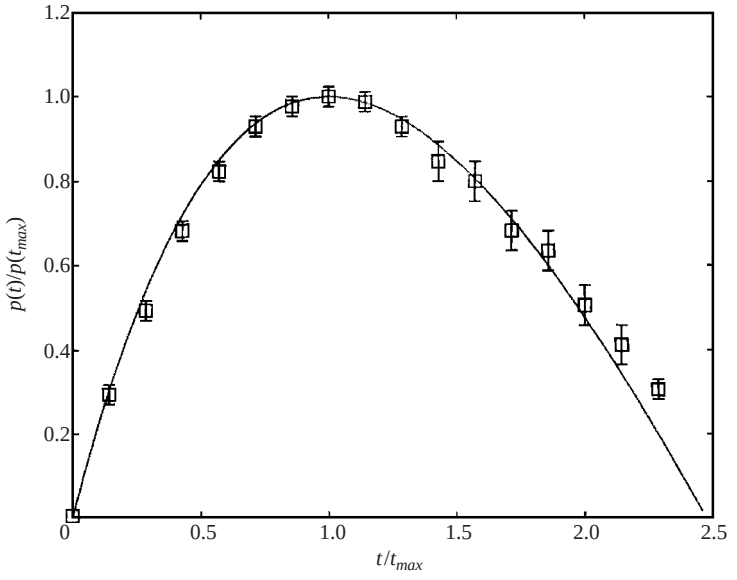

FIGURE 10. Penetration of a thermal plume from the more viscous layer as a function of time: squares show visually measured values for a given plume in experiment 22 (uncertainty is due to difficulties in precisely locating the maximum interface position and to possible parallax effects), and the line represents the fit according to (4.9) and (4.10). Because of entrainment, the final position of the interface is slightly higher than its initial position; after reconstruction of the outer thermal boundary layer, a new topography can develop.

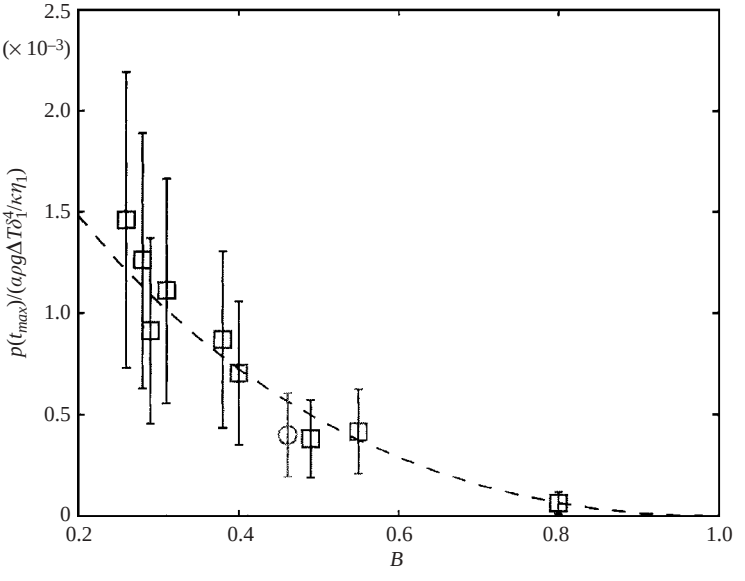

FIGURE 11. Evolution of the maximum penetration of the dynamic topography for experiments 16, 18, 19, 20, 21, 22, 25, 35, 37 (squares) and two-dimensional experiment 24 (circle). The dashed line represents the best fit according to (4.10): the experiments give a scaling factor $C_1 = 0.0031 \pm 0.0011$.

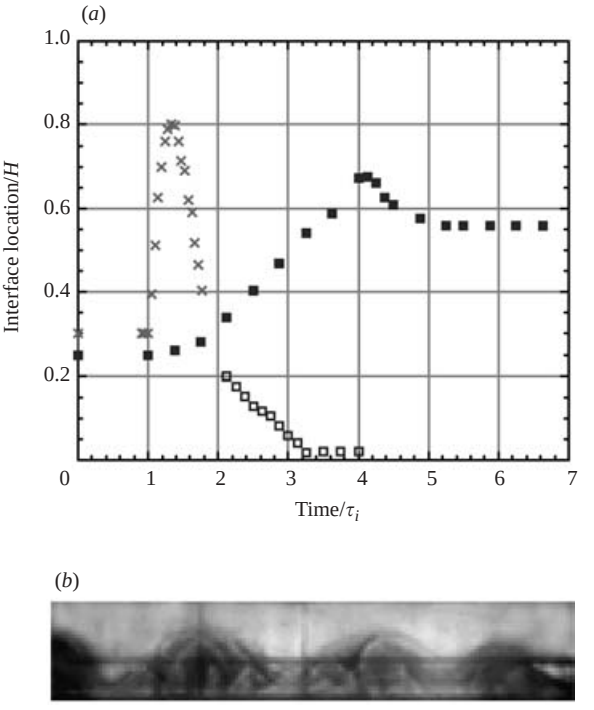

FIGURE 12. Dynamic topography in experiment 6: layer 1 is stagnant and progressively deformed by convection in layer 2. In (*a*) Filled and open squares respectively represent the evolution of the maximum and the minimum interface elevation as a function of time (normalized by the period of thermal plumes in layer 2). At time $t = 4\tau_2$, when the picture (*b*) was taken, layer 1 depth has reached a sufficient value for the local Rayleigh number to be critical. The evolution of dynamic topography driven by the most viscous layer in experiment 22 is also shown in (*a*) with $\times$; time is then normalized by the period of thermal plumes in layer 1.

5. Large-Rayleigh-number dynamics: characteristics of the large-scale thermochemical whole-layer regime

5.1. *Different types of whole-layer convection*

The whole-layer regime corresponds to the full destabilization of the system: it involves both layers, irrespective of their thermal history and their convective state. It is thus to be distinguished from the dynamic topography addressed in § 4. Close to marginal stability, two behaviours are possible as described in § 3: oscillations take place at relatively large B and/or low Ra and/or large viscosity ratio γ, and overturning takes place otherwise. The same observation is still relevant at large Ra, as shown in figure 13.

5.1.1. *Overturning*

When $1 \leqslant \gamma < 5$ typically (figure 13), the whole-layer regime takes the form of large convective features developing through the whole depth of the tank. The interface is distorted in all directions, and the two-layer initial system is never re-formed: overturning and immediate mixing occurs (see also Olson & Kincaid 1991).

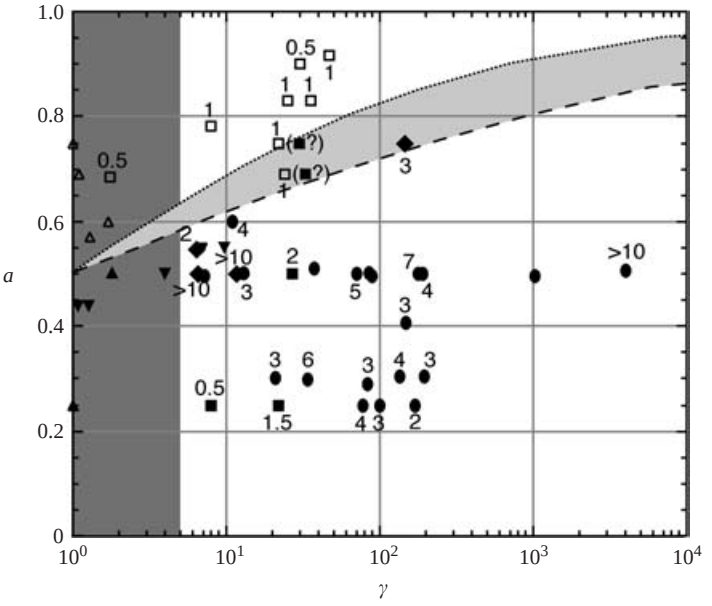

FIGURE 13. Observed behaviours of whole-tank convection as a function of viscosity and layer depth ratios: triangles stand for overturning and immediate mixing, diamonds for oscillations close to marginal stability, circles for 'vertical oscillations' and squares for 'initial configuration reversals'; the numbers near the symbols indicate the number of pulsations, from 0 to >10. The doming direction as defined in § 5.3 is also reported here: open symbols correspond to cavity plumes and filled symbols to diapiric plumes; the dotted line represents the theoretical law (5.14) $a = 1/(1+\gamma^{-0.2})$ from Ribe (1998) and the dashed line the theoretical law (5.16) $a = 1/(1+\gamma^{-1/3})$.

5.1.2. *Pulsations*

When $\gamma > 5$ typically, the whole-layer regime gives rise to large-scale oscillations: the two fluids preserve their own identity, and the initial two-layer system is periodically reconstructed. The number of observed pulsations rapidly increases with γ (figure 13). Two mechanisms of initial system reconstruction are possible, namely vertical oscillations and initial configuration reversals.

The typical evolution of vertical oscillations is presented in figure 14. Starting from an isothermal stratified system, the lower fluid is progressively heated and becomes lighter, whereas the upper fluid is cooled and becomes heavier (either by conduction or thermal convection in each layer). Once the chemical density anomaly is cancelled by thermal effects, the interface deforms in large domes that rapidly propagate until they reach the opposite boundary: fluid 1 near the cold plate becomes heavier whereas fluid 2 near the hot plate becomes lighter. The initial stratification finally reappears and the system goes back to its initial configuration. A new oscillation can begin. Stirring between the two layers of course slowly occurs by advection, but more than 10 successive pulsations have been observed.

Initial configuration reversals are presented in figure 15. They correspond to the behaviour predicted by Herrick & Parmentier (1994): the whole invading layer progressively migrates, until the initial configuration is totally reversed, with fluid 1 lying above fluid 2. Then, fluid 1 cools down, fluid 2 heats up, and the system finally goes back to the initial state. In this case, stirring also occurs by advection, but several successive reversals can be observed.

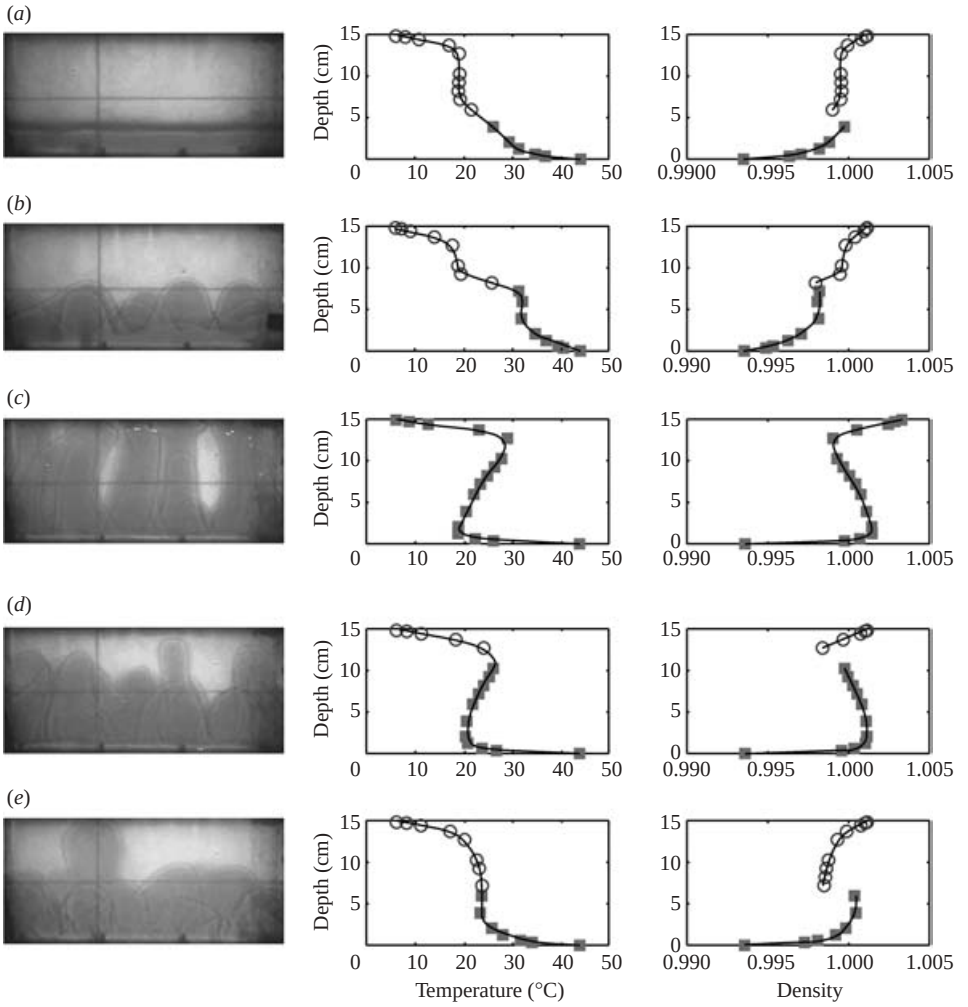

FIGURE 14. Whole-layer dynamics of experiment 18 in the form of vertical oscillations: pictures, instantaneous vertical temperature profiles measured by the vertical thermocouples probe, and deduced density profiles according to the equation of state $\rho_i(T) = \rho_{i0}(1 - \alpha(T)(T - T_0))$. Filled squares stand for thermocouples located in fluid 1, and open circles in fluid 2. (*a*) Initial configuration, just before destabilization ($t = 13.5$ min): the two layers are stratified. Convection characterized by a vertical temperature profile has developed in layer 2, whereas conduction takes place in layer 1. (*b*) Fluid 1 is now lighter than fluid 2, leading to a rising dome ($t = 16$ min). (*c*) The dome reaches the cold plate, where it progressively cools down and becomes heavier than the surrounding fluid 2 ($t = 20$ min). (*d*) It thus sinks ($t = 23$ min) and (*e*) finally goes back to its initial state ($t = 27.5$ min); another dome has risen in the background.

Vertical oscillations take place when domes cool down (respectively heat up) faster than they spread out in the vincinity of the cold plate (respectively hot plate), and rapidly collapse into the initial state: this thus occurs when the restoring force due to chemical stratification dominates the thermal buoyancy, that is when the buoyancy number is large ($B > 0.2$–0.3 typically, see figure 3) and/or the Rayleigh number relatively small. On the other hand, initial configuration reversals take place when the chemical stratification is low compared to the thermal buoyancy ($B < 0.2$ typically

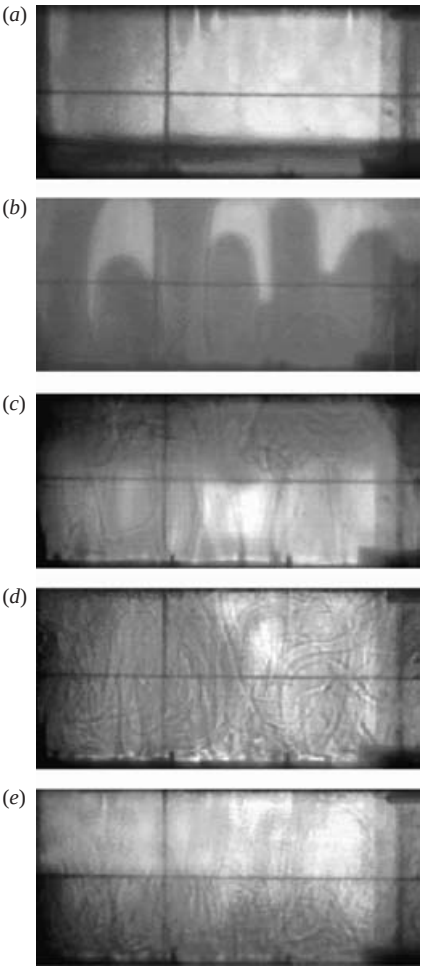

FIGURE 15. Whole-layer dynamics of experiment 9 in the form of initial configuration reversals. (*a*) Chemically stratified state, just before destabilization ($t = 9$ min). (*b*) Fluid 1 is now lighter than fluid 2, leading to rising domes ($t = 12$ min). (*c*) The layer 1 reforms under the cold plate, where it progressively cools down and becomes heavier; fluid 2 now corresponds to the lower layer and is progressively heated ($t = 14.5$ min). (*d*) The initial stratification finally reappears: both fluids go back to their initial position ($t = 17$ min) and (*e*) the chemically stratified system is re-formed ($t = 20.5$ min).

and/or large Ra), but also when the invading layer is small and thus rapidly emptied ($a < 0.3$ or $a > 0.7$, see figure 3).

5.2. *Onset of the whole-layer regime*

The whole-layer regime is excited when the thermal buoyancy is large enough to induce motions over the whole depth of the tank in spite of thermal diffusion, viscous drag and chemical stratification. The details of its onset depend on the initial conditions in the system.

5.2.1. *Initial buoyancy ratio lower than critical*

When the buoyancy number is lower than the critical value determined by marginal stability, the whole-layer regime is the most unstable thermochemical mode (see

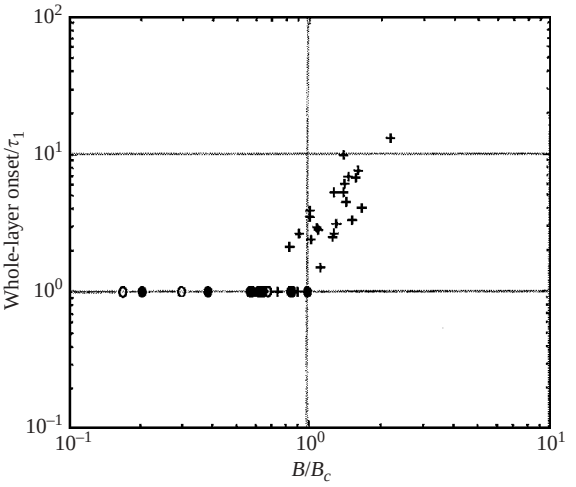

FIGURE 16. Onset time for whole-layer convection divided by the purely thermal convective time in the most viscous layer, as a function of the buoyancy number normalized by the critical buoyancy number determined with marginal stability analysis. Circles stand for 'marginally unstable' experiments (open symbols correspond to experiments where the less viscous layer invades the most viscous one): the time ratio is then equal to 1 by construction. + stand for 'marginally stable' experiments that are finally destabilized.

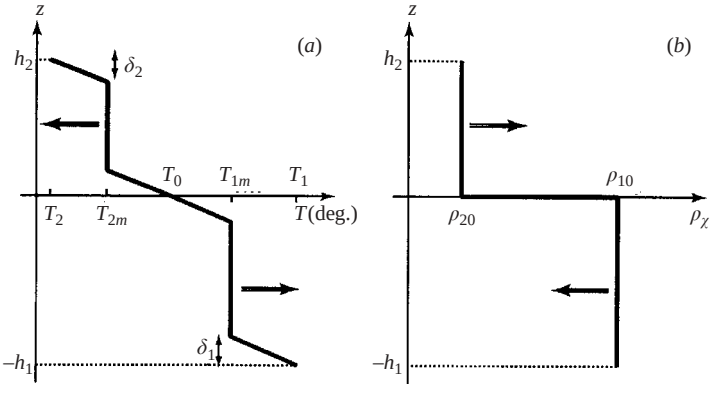

FIGURE 17. Sketches of (*a*) the temperature profile and (*b*) the chemical density profile at large Rayleigh numbers; arrows indicate the temporal evolution.

Le Bars & Davaille 2002). Starting from isothermal fluids, we observed in all corresponding experiments that (i) thermal convection first starts in the less viscous layer 2, but is not sufficient to induce whole-layer motions; (ii) the thermochemical regime is excited as soon as heat is transferred through the most viscous layer, either by conduction or thermal convection. The thermochemical onset time is therefore equal to the onset time of the purely thermal mode in layer 1 (figure 16).

5.2.2. *Initial buoyancy ratio greater than critical*

When $B > B_c(\gamma, a)$, the configuration is 'marginally stable': the linear study predicts a stratified regime with a stable interface. This is indeed observed experimentally, at least for a few overturns. However, at high Rayleigh numbers the system evolves over time and is finally destabilized (figure 16), as sketched in figure 17: the

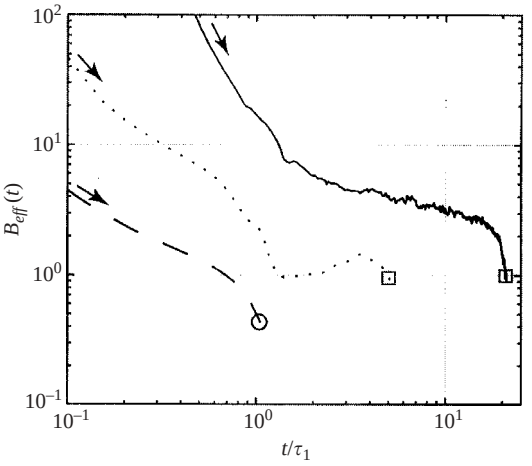

FIGURE 18. Time evolution of the effective buoyancy number until interface destabilization for experiments 8 (marginally unstable: dashed line), 28 (marginally stable, but destabilized after 1 hour, once the temperature contrast at the interface has reached a sufficient value: dotted line) and 910 from Davaille (1999*a*) (marginally stable, but destabilized after 8.5 hours because of thermal evolution and mixing at the interface: solid line).

temperature is almost constant through the core of each convecting layer, and a thermal boundary layer develops around the interface with a temperature jump that gradually increases (Herrick & Parmentier 1994); thermal convection in each layer induces entrainment across the interface by viscous coupling (Davaille 1999*a*), which continuously decreases the chemical stratification.

In this context, a first-order approach consists in ignoring the effective thermal and chemical variations and only considering a constant mean density in each layer with a sharp change at the interface:

$$\overline{\rho_i} = \rho_{i0} - \overline{\alpha\rho_0(T - T_0)}_i, \tag{5.1}$$

where $\overline{\alpha\rho_0(T - T_0)}_i$ is the mean value of thermal buoyancy $\alpha\rho_0(T - T_0)$ over the layer i. Such a system is then comparable to Rayleigh–Taylor configurations (see for instance Whitehead & Luther 1975) and becomes unstable provided

$$\overline{\rho_1} < \overline{\rho_2}. \tag{5.2}$$

In terms of buoyancy number, (5.2) means that the effective buoyancy number based on real chemical and thermal contrasts:

$$B_{eff}(t) = \frac{\Delta\rho_\chi(t)}{\overline{\alpha\rho_0(T - T_0)}_1 - \overline{\alpha\rho_0(T - T_0)}_2} \tag{5.3}$$

becomes strictly lower than 1.

In the experiments, B_{eff} can be calculated using the vertical thermocouples probe to measure the effective thermal buoyancy and scaling laws from Davaille (1999*a*) to estimate the evolution of the effective chemical density contrast. As shown in figure 18, destabilization indeed takes place for B_{eff} slightly smaller than 1: the mean experimental value at onset is

$$B_{eff} = 0.98 \pm 0.12 \tag{5.4}$$

for $0.51 < a < 0.83$, $1.3 < \gamma < 25$ and $1.7 \times 10^6 < Ra < 7.5 \times 10^7$.

This simplified model focuses on the influence of the chemical stratification on the destabilization: for the whole-layer regime to be excited, thermal effects have to reverse the initial density contrast. These are indeed the predominant effects at large Ra–large B. However, the model implicitly neglects thermal and viscous diffusion during motions over the whole depth of the tank. A more complete analytical model can be proposed following Herrick & Parmentier (1994): the buoyancy effectively available for motions over the whole depth of the tank is given by

$$\Delta\rho_{eff} = \overline{\rho_2} - \overline{\rho_1} = [\overline{\alpha\rho_0(T - T_0)}_1 - \overline{\alpha\rho_0(T - T_0)}_2] - \Delta\rho_\chi(t). \tag{5.5}$$

Whole-layer motions are mainly governed by the most viscous fluid: therefore, we define the Rayleigh number characteristic of interface destabilization as

$$Ra_{eff} = \frac{\Delta\rho_{eff} g H^3}{\kappa\eta_1}. \tag{5.6}$$

Whole-layer motions are excited when Ra_{eff} reaches the critical value of one-layer convection with rigid boundaries $Ra_c = 1707.76$ (Chandrasekhar 1961), which means that $\Delta\rho_{eff}$ reaches the critical value

$$\Delta\rho_c = \frac{Ra_c}{Ra}\alpha\rho_0\Delta T\gamma. \tag{5.7}$$

The chemical evolution of the system can be modelled using the scaling laws defined by Davaille (1999*a*): it takes place on a much longer time scale that the thermal evolution, as observed in the experiments (see figure 18 for instance). One can thus separate two trends. (i) A medium-term thermal evolution: the chemical density anomaly can then be taken as a constant and (5.7) means that the effective buoyancy number has to reach a critical value

$$B_c = \frac{1}{1 + (\gamma/B)Ra_c/Ra}. \tag{5.8}$$

(ii) A long-term chemical evolution: one can then consider that the thermal evolution of the system has reached a steady state. For instance, the heat balance for the idealized situation sketched in figure 17 implies

$$\frac{T_1 - T_{1m}}{\delta_1} = \frac{T_{1m} - T_{2m}}{\delta_1 + \delta_2} = \frac{T_{2m} - T_2}{\delta_2}, \tag{5.9}$$

where T_{im} is the mean interior temperature of layer i and δ_i is the thermal boundary layer thickness, so

$$T_{1m} - T_{2m} = \frac{\Delta T}{2}. \tag{5.10}$$

For the long term, we can thus write

$$\overline{\alpha\rho_0(T - T_0)}_1 - \overline{\alpha\rho_0(T - T_0)}_2 = \epsilon\alpha\rho_0\Delta T \tag{5.11}$$

where ϵ is a constant that depends on the variations of $\alpha(T)$ ($\epsilon = 1/2$ if α is constant). Equation (5.7) then means in terms of effective buoyancy number that

$$B_c = 1 - \epsilon\gamma\frac{Ra_c}{Ra}. \tag{5.12}$$

Equations (5.8) and (5.12) thus complete the condition $B_{eff} < 1$ given previously in introducing thermal diffusion and mechanical dissipation in the condition for destabilization. However, both conditions tend quite quickly towards 1, and the error

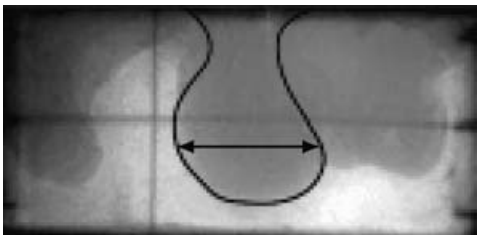

FIGURE 19. Cavity plume in experiment 31, where the invading layer is the less viscous: the arrow shows the measured diameter 9.3 ± 1.0 cm for a theoretical value given by (5.19) of 10.3 ± 2.1 cm.

bars on our measured B_{eff} do not allow us to recover experimentally the expected dependence.

From a general point of view, we conclude that the onset of whole-layer convection at high Rayleigh number occurs whenever the more viscous layer convects and $B_{eff} < 1$.

5.3. *A Rayleigh–Taylor-type destabilization: shapes and direction of doming*

As observed in the closely related case of Rayleigh–Taylor instabilities (Whitehead & Luther 1975), the pattern of destabilization depends on the direction of doming: in most experiments, we observe domes developing from the most viscous fluid into the less viscous one in the form of large cylinders called 'diapiric plumes' separated by cusps (figures 14 and 15). In some cases however, those cusps transform into active sinking features, in the form of large blobs followed by a thinner tail, comparable to cavity plumes (figure 19).

In Rayleigh–Taylor instabilities, the direction of "spouting" (Ribe 1998) (i.e. superexponential growth of interfacial extrema) is determined by the relative value of two parameters, characterizing the 'penetrability' of each layer: the viscosity ratio, since it is easier to penetrate a less viscous layer; the layer depth ratio, since it is easier to invade a deeper layer, where boundary conditions do not limit motions. For 'rigid' boundary conditions, the "spouting" direction changes when

$$\frac{h_1}{h_2} = \left(\frac{\nu_1}{\nu_2}\right)^{0.2} \tag{5.13}$$

(Ribe 1998, private communication), which means with our notation

$$a = \frac{1}{1+\gamma^{-0.2}}. \tag{5.14}$$

In our configuration, the destabilization is due to thermal transfer, which must therefore be taken into account. Consider a buoyant particle located at the interface: its ability to reach the i boundary is measured by Ra_i, the ratio of buoyancy to thermal and viscous diffusive effects through the fluid i (see for instance Turner 1979, pp. 208–209). Once the interface is unstable, its deformation will tend to develop through the layer where motion is easier, thus through the layer with the highest Ra_i. The doming direction thus changes when

$$Ra_1 = Ra_2, \tag{5.15}$$

which means at first order

$$\frac{h_1}{h_2} = \left(\frac{\nu_1}{\nu_2}\right)^{1/3} \Leftrightarrow a = \frac{1}{1+\gamma^{-1/3}}. \tag{5.16}$$

As described by Ribe (1998), the higher exponent in (5.16) than in (5.14) corresponds to an increased influence of the viscosity ratio: in the Rayleigh–Taylor calculations, the configuration is inherently unstable and viscosities only influence the 'penetrability'. In our proposed first-order approach, viscosities have a twofold influence: they act on the 'penetrability', but also control heat transfers, which are responsible for the interface destabilization.

Experimental observations reported in figure 13 indicate a dependence on a and γ in agreement with (5.14) and (5.16), but do not allow a choice to be made between the two proposed coefficients.

5.4. *Characteristic wavelength and diameter*

The selected wavelength in our configuration is totally different from Rayleigh–Taylor instability (figure 20*a*). Initial perturbations of the interface are due to thermal transfers from the hot and cold plates. Since the largest temperature fluctuations come from the most viscous fluid, this also controls the wavelength of doming: figure 20(*b*) thus exhibits a slight dependence on Ra_1 corresponding to the experimental law

$$\frac{\lambda}{h_1} = 9.1 Ra_1^{-0.14}, \tag{5.17}$$

accurate for both directions of doming with a typical precision of 20%.

As observed in figure 21, the diameter of diapiric plumes scales as

$$\frac{\lambda}{d_{dia}} = 2.0 \pm 0.3. \tag{5.18}$$

Measurements for cavity plumes are more difficult since our tank is not large enough to observe more than 2 or 3 successive structures and not long enough for the expected spherical shape with a fixed diameter d_{cav} to fully develop before reaching the opposite plate. A simple volume conservation of fluid 2 however gives

$$4/3\pi(d_{cav}/2)^3 \sim \lambda^2 h_2 \tag{5.19}$$

that seems to indicate the relevant order of magnitude (see figure 19 for instance).

In both cases, we note that when purely thermal plumes exist in the layer before doming, each dome collects several small-scale instabilities.

5.5. *Typical velocities*

Since inertial effects are negligible, convective motions are controlled by the equilibrium between buoyancy effects and viscous drag forces. When both layers are involved, drag forces are dominated by the most viscous fluid (Whitehead & Luther 1975): the scaling analysis then gives a typical domes velocity

$$w \sim \frac{\Delta\rho_{eff} g d^2}{\eta_1}, \tag{5.20}$$

where d is a typical size of the dome and $\Delta\rho_{eff}$ the density contrast available for motion over the whole depth as given by (5.5), taking into account both thermal and chemical effects.

Figure 22 presents measurements for two examples. Cavity plumes exhibit a constant velocity (figure 22*a*), which can be compared to (5.20) using measured $\Delta\rho_{eff}$

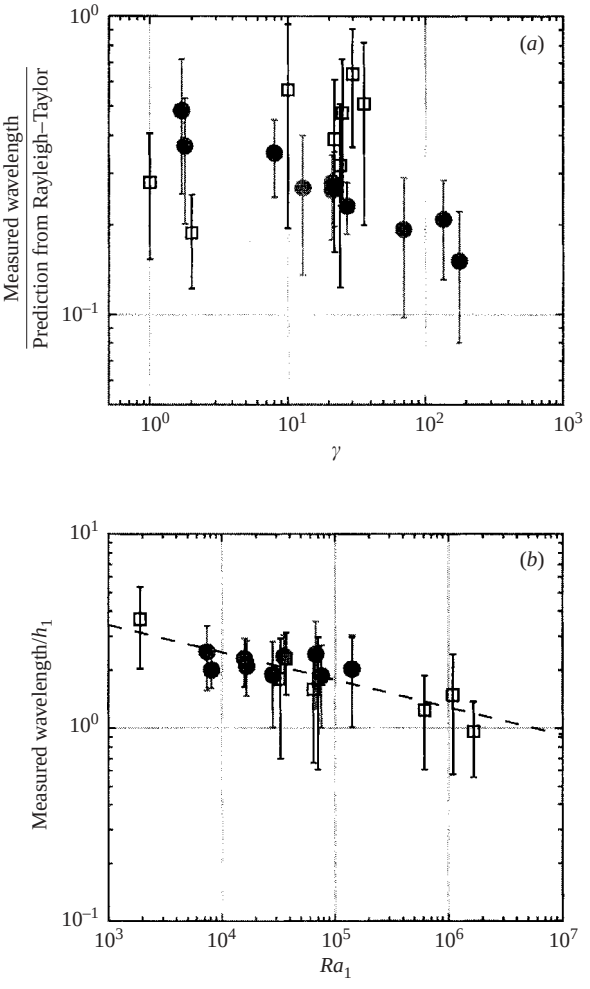

FIGURE 20. (*a*) Wavelength of diapiric plumes (filled circles) and cavity plumes (squares) normalized by the predictions for Rayleigh–Taylor instabilities ($\lambda = 4\pi h_1(\gamma/180)^{1/5}$ in the case of $a \ll 1$ and $\gamma \gg 1$ and $\lambda = 2\pi h_2(\gamma/3)^{1/3}$ in the case of a close to 1 and $\gamma \gg 1$, Ribe 1998): theoretical values for Rayleigh–Taylor instabilities do not indicate the relevant parameter dependence. (*b*) Wavelength of diapiric plumes (filled circles) and cavity plumes (squares) normalized by the depth of the most viscous layer as a function of the most viscous layer Rayleigh number: heat transfers in fluid 1 control the initial perturbations at the interface, and thus the selected wavelength.

and $d = d_{cav}$: results are presented in figure 23. In the case of diapiric plumes, the development can be divided in two steps (figure 22*b*):

(i) During an 'initiation' stage, the diameter of the interface deformation progressively increases with the height and the velocity is mainly constant. The theoretical value (5.20) can then be calculated from measured $\Delta\rho_{eff}$ and $d = d_{dia}$ (see figure 23).

(ii) Once the interface deformation reaches a value comparable to d_{dia}, a 'maturation' stage starts: the deformation takes the form of a cylinder with a nearly constant diameter. The characteristic length that must be used in (5.20) is intermediate between the height of the plume h and d_{dia}, and the rising speed rapidly increases with h.

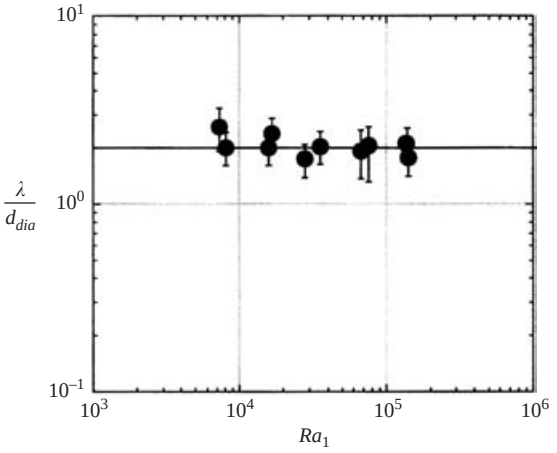

FIGURE 21. Ratio of wavelength to diameter of diapiric plumes as a function of the most viscous layer Rayleigh number: the line shows the mean value 2.0 ± 0.3.

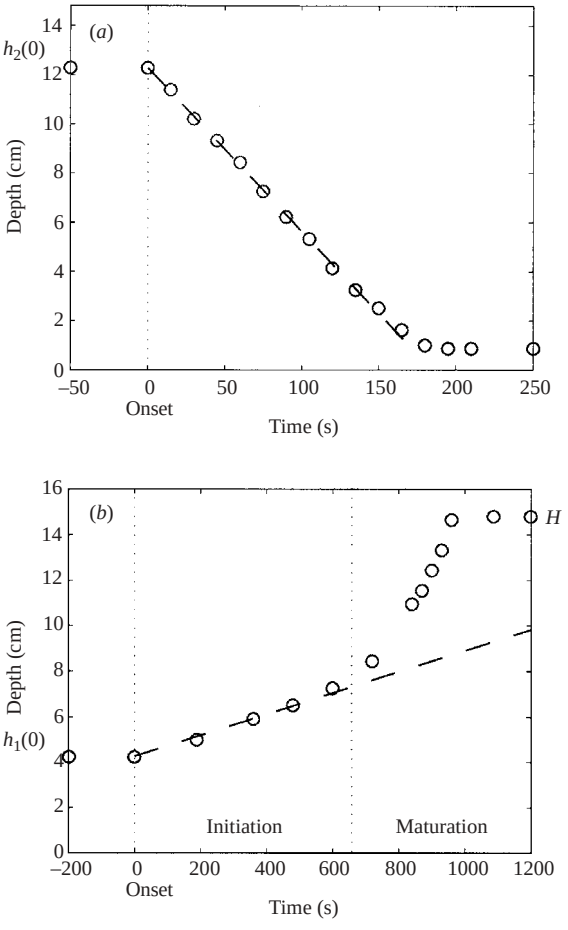

FIGURE 22. Position of the interface as a function of time for (*a*) a cavity plume in experiment 27 (measured velocity $w = -4.0\,\mathrm{cm\,min^{-1}}$, dashed line) and (*b*) a diapiric plume in experiment 10 (measured initial velocity $w_{init} = 0.33\,\mathrm{cm\,min^{-1}}$, dashed line).

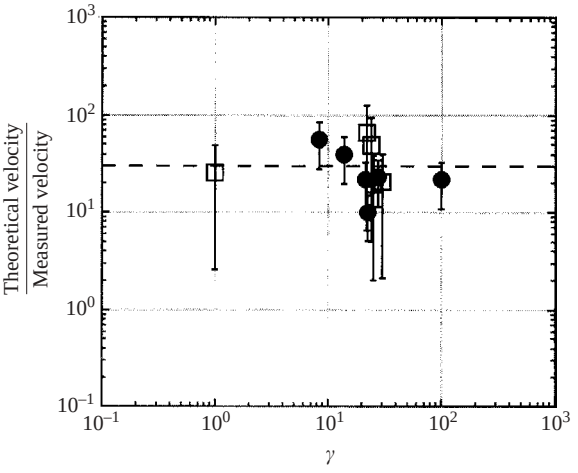

FIGURE 23. Ratio of the theoretical velocity given by (5.20) to the measured velocity of diapiric plumes (filled circles) and cavity plumes (squares): the dashed line corresponds to a scaling factor $C_3 = 1/(32 \pm 18)$.

This behaviour is reminiscent of the ascent of diapirs created by injection of a buoyant viscous fluid through a small orifice, presented by Olson & Singer (1985): a coefficient $\ln(h/d_{dia})$ was then introduced in (5.20) to take into account the cylindrical morphology. In our experiments however, the relatively small depth of the tank as well as the large error bars on the theoretical speed do not allow such a dependence to be recovered.

As shown in figure 23, both the initial velocities of diapiric plumes and the constant velocities of cavity plumes are consistent with a scaling factor

$$C_3 = \frac{1}{32 \pm 18}. \tag{5.21}$$

The large scattering is mainly due to the difficulties in measuring $\Delta\rho_{eff}$ and d_{cav} (see § 5.2 and § 5.4).

5.6. *Pulsation periods at large viscosity ratio*

As described in § 5.2, the interface is destabilized when thermal effects are large enough to induce whole-tank motions in spite of thermal and mechanical diffusion as well as chemical stratification: for the initial destabilization, this means that the thermal density contrast between the two fluids has to increase from 0 (initially isothermal fluids) to the critical value $\Delta\rho_\chi + \Delta\rho_c$, where $\Delta\rho_c$ depends on viscous and thermal diffusions (see § 5.2). Then, the chemical signal $\Delta\rho_\chi$ remains stable, and the further rising and sinking motions correspond only to the gain and loss of the 'dynamic' part of the density difference $\Delta\rho_c$ (Herrick & Parmentier 1994): this is mainly controlled by the fluid with greater viscosity, which slows down the whole process. We can thus scale the observed pulsation periods at large viscosity ratio with the characteristics of layer 1. It turns out that the dependence is similar to the case of purely thermal convection:

$$t_{pulsation} = \frac{h_1^2}{\pi\kappa}\left(\frac{Ra_c}{Ra_1}\right)^{2/3}, \tag{5.22}$$

where the experimental determination of Ra_c gives $Ra_c = 880 \pm 170$ (figure 24). Thermal plumes in layer 1 and thermochemical features have similar periodicities.

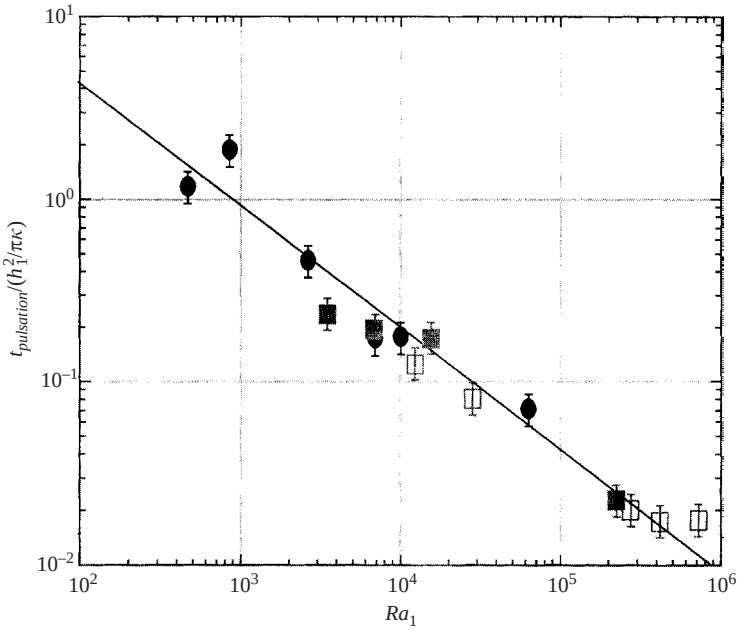

FIGURE 24. Observed period of initial system reconstruction depending on the Rayleigh number of the layer with greater viscosity. Circles denote 'vertical oscillations' and squares 'initial configuration reversals'; open symbols correspond to cavity plumes and filled symbols to diapiric plumes. The line shows the best fit according to (5.22): $Ra_c = 880 \pm 170$.

However, the critical Rayleigh number for whole-layer motions is smaller, in agreement with marginal stability analysis that predicts the whole-layer regime to be the most unstable (see Le Bars & Davaille 2002). Moreover, these two convective features act on totally different length scales, since several small-scale thermal plumes are collected inside each large-scale thermochemical structure (see § 5.4).

6. Time evolution: from whole-layer to one-layer convection

Once the two-layer system is destroyed, thermochemical heterogeneities are dispersed over the whole volume of the tank: the mixture can then be considered as a single equivalent fluid, characterized by a complicated viscosity, strongly spatially variable and an 'internal' temperature field due to the thermal compensation of the chemical stratification between fluids 1 and 2.

Examining the destabilization of the outer thermal boundary layers, we note that the local viscosity of the equivalent fluid ν_{local} depends on the local proportion of fluids 1 and 2, and can thus range between ν_1 (fluid 1 alone) and ν_2 (fluid 2 alone). Since the excited period depends on $\nu_{local}^{2/3}$ (Howard 1964), a noisy wavelet analysis is recorded (figure 25*c*). Moreover, as described in § 5.6, the 'chemical' signal $\Delta\rho_\chi$, corresponding to the temperature variation

$$\frac{\Delta\rho_\chi}{\alpha\rho} = B\Delta T, \tag{6.1}$$

is stable, and does not act on convective motions that are controlled by additional

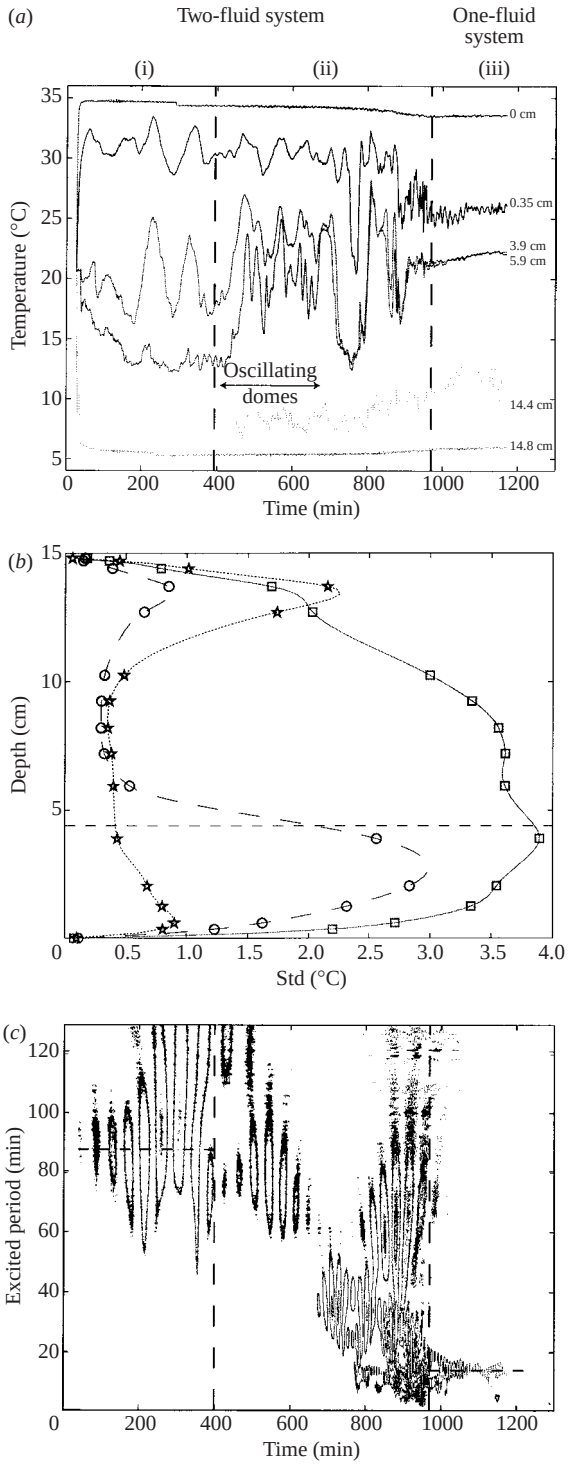

FIGURE 25. For caption see facing page.

fluctuations: the passage of a particle of fluid 1 anywhere in the tank thus differs from the passage of a particle of fluid 2 by $B\Delta T$, explaining the presence of large temperature variations over the whole depth (figure 25*b*).

Local stirring and ultimately chemical diffusion progressively annihilate the chemical difference between the two fluids, and thus the associated temperature difference: the usual configuration finally returns, characterized by fluctuations limited to the thermal boundary layers (figure 25*b*) and two excited periods only, corresponding to plumes from hot and cold plates. At large local Rayleigh number ($\widetilde{Ra_i} > 10^4$ typically), their periods scale as (Howard 1964)

$$\tau_i = \frac{H^2}{\pi\kappa}\left(\frac{Ra_c}{\widetilde{Ra_i}}\right)^{2/3}, \tag{6.2}$$

where

$$\widetilde{Ra_i} = \frac{\alpha_i g \Delta T_i H^3}{\kappa \nu_{mixed}}. \tag{6.3}$$

Here, ν_{mixed} corresponds to the viscosity of the 'mixed' solution, ΔT_i is the temperature contrast through the boundary layer i and α_i is the thermal expansion coefficient at the mean temperature of the boundary layer i. The critical Rayleigh number determined experimentally $Ra_c = 1100 \pm 500$ (figure 26) is in close agreement with the theoretical value for 'free–rigid' boundary conditions of 1100.7 (Pellew & Southwell 1940) and with the value determined in § 4.1 for the onset of thermal convection inside each layer.

The overall duration of thermochemical heterogeneities is very difficult to determine, since all the dimensionless numbers directly influence it: the buoyancy number controls the 'chemical' resistance to stirring, the viscosity ratio the 'mechanical' resistance to stirring, the layer depth ratio the relative volume of heterogeneities and the Rayleigh number the convective stirring power. Studying the variation of the overall duration with all dimensionless numbers is beyond the scope of this paper. Moreover, with our experimental set-up, only the buoyancy number can be changed independently of all other parameters: as shown in figure 27, the overall duration then exhibits a strong exponential dependence on B. The chemical heterogeneities can thus persist for very a long time compared to the characteristics of thermal convection.

FIGURE 25. Time evolution of experiment 20. (*a*) Temperature signals recorded by six thermocouples located on the vertical probe: their location is given on the right (initial interface position: 4.4 cm). The time history can be divided in three parts: (i) the stratified phase, where purely thermal convection develops above and below a stable interface; (ii) the whole-layer phase, where the interface is destabilized and whole-tank convection takes place; (iii) the final one-layer phase, where the interior of the tank is well mixed (classical Rayleigh–Bénard convection). (*b*) Standard deviation of the temperature signal (measured by the vertical probe) as a function of depth: circles correspond to the stratified phase (weak convection in layer 1, strong convection in layer 2), squares to the whole-layer phase and stars to the final one-layer phase. (*c*) Wavelet analysis of the temperature signal in the hot thermal boundary layer (thermocouple located at 0.35 cm from the hot plate): contours follow most excited periods.

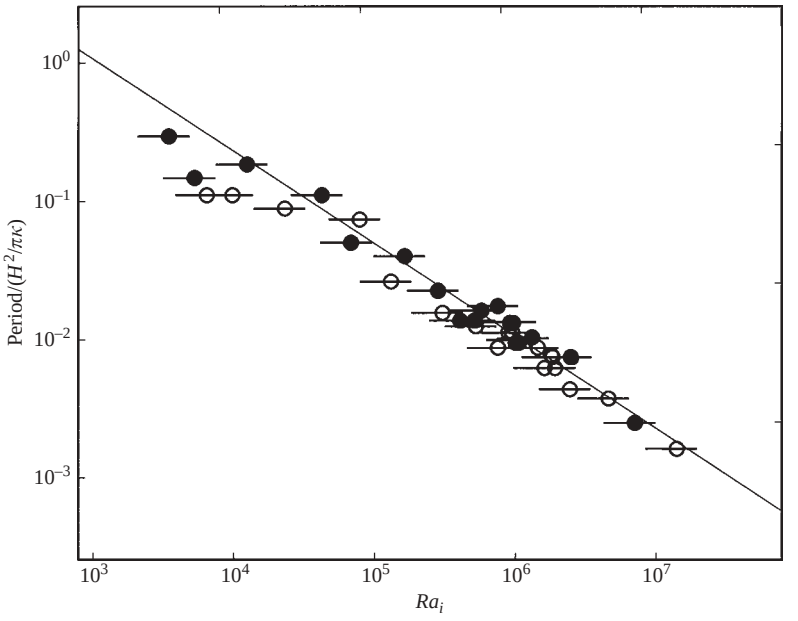

FIGURE 26. Plume period measured after mixing in the vicinity of the cold plate (filled) and of the hot plate (open) as a function of the local Rayleigh number. Plume period is defined as the mean period of temperature fluctuations in the corresponding thermal boundary layer, as measured by the vertical thermocouple probe. The line corresponds to the best fit according to (6.2), only taking into account experiments where $\widetilde{Ra_i} > 10^4$: the experimental critical value is $Ra_c = 1100 \pm 500$.

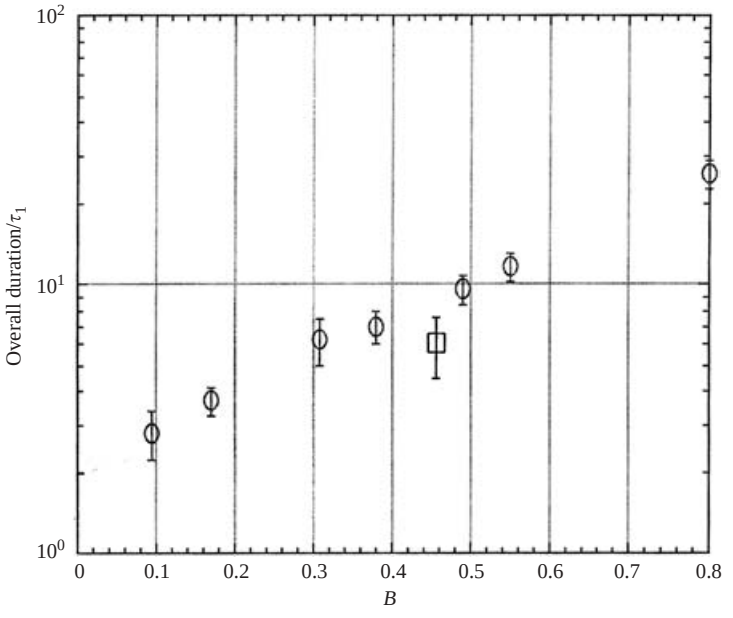

FIGURE 27. Overall duration of chemical heterogeneities normalized by the typical convective time in layer 1 as a function of B for experiments 9, 13, 18, 19, 20, 21, 22 (circles) and two-dimensional experiment 24 (square): in these experiments, only the buoyancy number significantly changes ($\gamma = 8$–22, $a = 0.25$–0.30, $Ra = 4.1 \times 10^6$–1.5×10^7).

7. Conclusion

At large Rayleigh number, motions in a two-fluid system are due to three distinct phenomena: purely thermal convection inside layer 1; purely thermal convection inside layer 2; and large-scale thermochemical convection, where both layers are involved.

Experiments reported in this paper supplement the study of the two-layer Bénard problem in the particular case where the interface between the two fluids greatly deforms. Two different mechanisms have been described:

(i) dynamic topography appears from the local and partial intrusion into one fluid of purely thermal features from the other one;

(ii) a Rayleigh–Taylor-type overturn takes place at the interface when the system is unstable according to marginal stability ($B \leqslant B_c(\gamma, a)$, see Le Bars & Davaille 2002), or when the most viscous layer convects and the effective buoyancy number based on the real chemical and temperature profiles becomes lower than 1.

Both regimes are transient and systematically evolve towards one-layer Rayleigh–Bénard convection. Heterogeneity is however registered over very long times compared to typical time scales of thermal convection. Further experiments are now necessary to understand and quantify the influence of viscosity and density contrasts on mixing processes of such active heterogeneities.

This work benefited from fruitful discussions with Claude Jaupart, Damien Jurine, Peter Molnar, Jeffrey Park, Neil Ribe, Harro Schmeling and George Veronis. It also benefited from the constructive comments of Henri-Claude Nataf and an anonymous reviewer. A.D. is grateful to Yale University for its hospitality. This research has been supported by the French INSU programs IDYL and IT. This is an IPGP contribution.

Appendix A. Physical properties of the fluids

Working fluids are essentially water, to which small amounts ($< 2\%$) of a cellulose called natrosol are added (Tait & Jaupart 1989): their physical properties are thus comparable to water (for instance, $\kappa = 1.42 \times 10^{-7}\,\mathrm{m^2\,s^{-1}}$), except for density and viscosity (figure 28). Small amounts of salt ($<7\,\mathrm{kg\,m^{-3}}$) can also be added to independently control the density of the mixture. Those solutions are totally miscible, eliminating the unwanted effect of surface tension at the interface, and remain Newtonian for the low deformation rates associated with the velocity of convective features in the tank. The coefficient of thermal expansion and the viscosities are temperature-dependent (figure 29): unless otherwise stated, we use values at the initial mean temperature of the tank (20°C), which is relevant for global processes such as the whole-layer regime (see Appendix B); for local processes however, as for instance thermal boundary layer instabilities, values at the local temperature are used. Viscosity contrasts between the two layers are taken at the interface, thus at a given temperature.

Appendix B. Influence of the variations of the thermal expansion coefficient

In addition to the marginal stability study presented in Le Bars & Davaille (2002), we can study the case where thermal expansion coefficients of layers 1 and 2 are different (respectively α_1 and α_2). The density profile corresponding to the linear

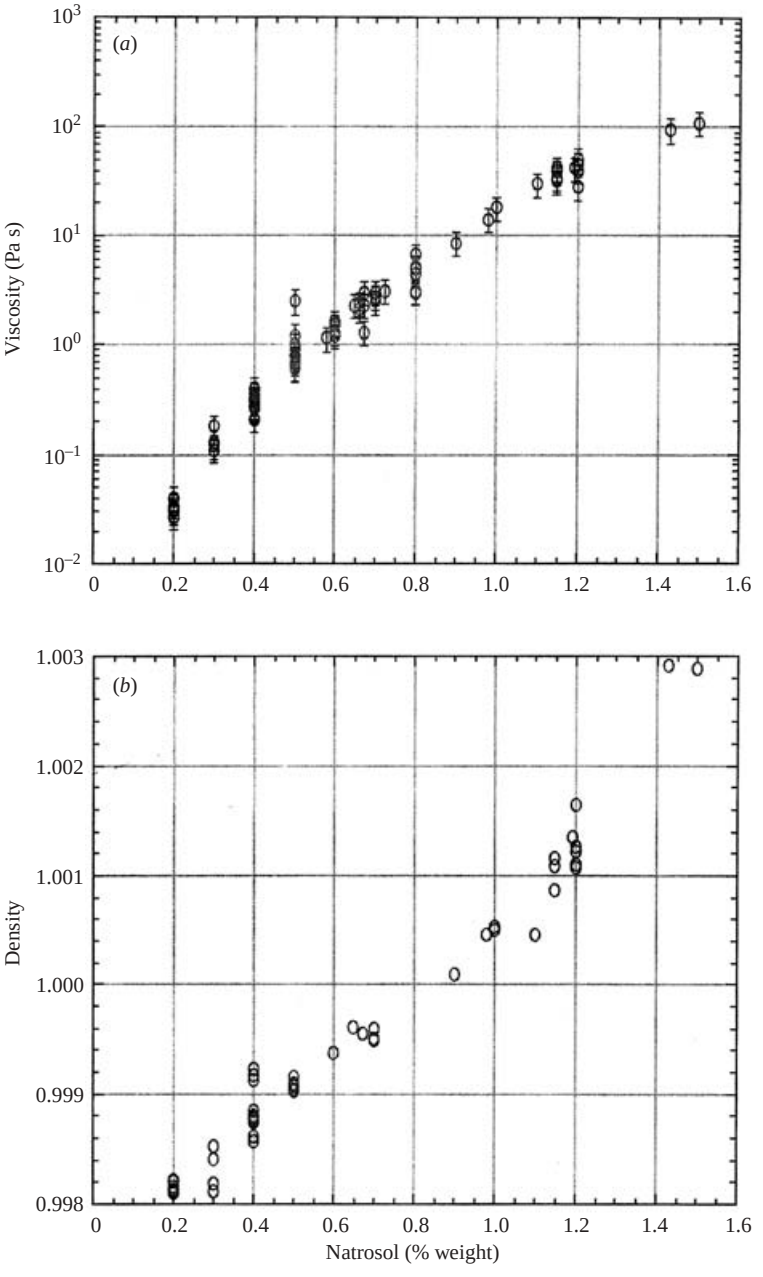

FIGURE 28. (*a*) Viscosity (measured with a rotoviscosimeter Haake RV20) and (*b*) density (measured with a densimeter Anton Paar DMA 5000) of the working fluids at 20°C as a function of the percentage in weight of cellulose (no salt).

temperature profile is

$$\rho_i = \rho_{i_0} - \alpha_i \rho_0((T_1 - T_0) - (z + a)\Delta T), \tag{B 1}$$

where z is the height non-dimensionalized by H. The effective density contrast at the

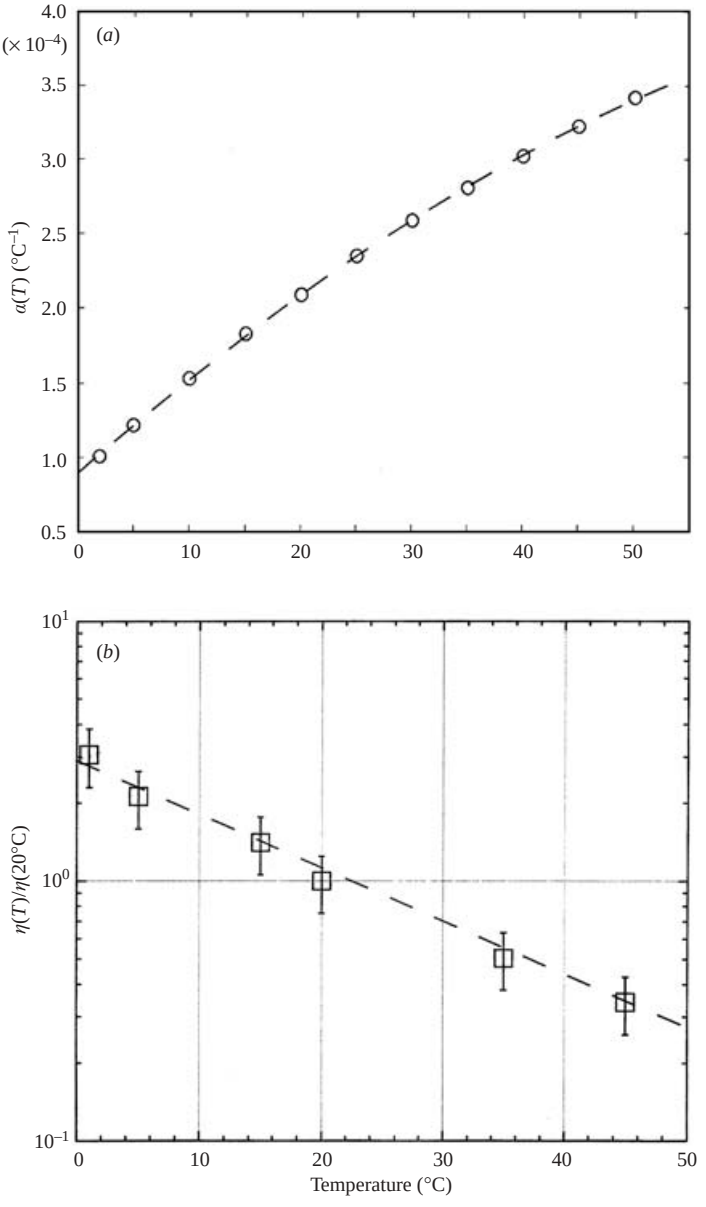

FIGURE 29. Temperature-dependence of (*a*) the coefficient of thermal expansion and (*b*) the viscosity. Dashed lines represent experimental fits: $\alpha(T) = -3.1\times10^{-8}T^2 + 6.6\times10^{-6}T + 8.9\times10^{-5}$ and $\eta(T)/\eta(20\,^\circ\mathrm{C}) = 2.45\mathrm{e}^{-0.045T}$, where T is the temperature in °C.

interface ($z = 0$), taking into account both thermal and chemical effects, is then

$$\Delta\rho_{interface} = \Delta\rho_\chi + (\alpha_2 - \alpha_1)\rho_0((T_1 - T_0) - a\Delta T). \tag{B 2}$$

In particular, one can note that

$$\Delta\rho_{interface} < 0 \iff B < \left(\frac{T_1 - T_0}{\Delta T} - a\right)\left(\frac{\alpha_1}{\alpha_2} - 1\right), \tag{B 3}$$

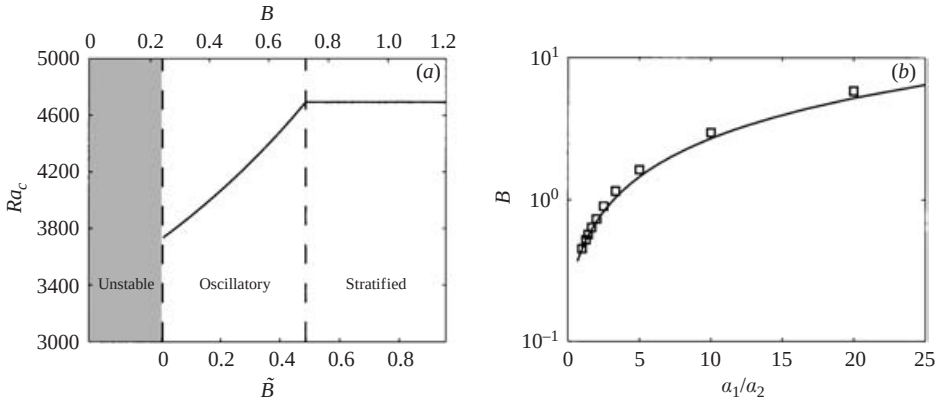

FIGURE 30. (*a*) Neutral curves of marginal stability analysis as a function of B and $\widetilde{B}$ in the case $\alpha_1/\alpha_2 = 2$, $\gamma = 10$, $a = 0.25$. (*b*) B_c as a function of α_1/α_2 for $\gamma = 10$, $a = 0.25$: squares show calculated points and the solid line indicates the fit according to the law (B 7).

where

$$B = \frac{\rho_{1_0} - \rho_{2_0}}{\alpha_2 \rho_0 \Delta T}. \tag{B 4}$$

The density profile is then unstable independently of convective effects, and the critical Rayleigh number is equal to 0 (figure 30*a*).

The main control parameter in a two-layer system is the buoyancy number B that appears in the continuity of normal stress (see equation (2.13) of Le Bars & Davaille 2002). In the present configuration, B is remplaced by

$$\widetilde{B} = B + \left(\frac{T_1 - T_0}{\Delta T} - a\right)\left(1 - \frac{\alpha_1}{\alpha_2}\right). \tag{B 5}$$

As a first approximation, we can ignore changes in α and use results from Le Bars & Davaille (2002) by replacing B with $\widetilde{B}$ (figure 30*a*). Then: a chemically unstable density profile, given by $B < 0$ when α is constant, now corresponds to $\widetilde{B} < 0$: this condition is similar to (B 3); the critical value $\widetilde{B}_c$ separating stratified and whole-layer regimes depends of γ and a, but is almost independent of α_1/α_2. We then deduce from (B 5) that

$$\widetilde{B}_c = B_c\left(\frac{\alpha_1}{\alpha_2} = 1\right) \tag{B 6}$$

and so

$$B_c\left(\frac{\alpha_1}{\alpha_2}\right) = B_c\left(\frac{\alpha_1}{\alpha_2} = 1\right) + \left(\frac{T_1 - T_0}{\Delta T} - a\right)\left(\frac{\alpha_1}{\alpha_2} - 1\right), \tag{B 7}$$

in good agreement with numerical results (figure 30*b*).

This simple linear study thus indicates that the physics of the problem is independent of the explicit variations in $\alpha(T)$: in our experiments, its mean value is used.

REFERENCES

Andereck, C. D., Colovas, P. W. & Degen, M. M. 1996 Observations of time-dependent behaviour in the two-layer Rayleigh-Bénard system. In *Advances in Multi-Fluid Flows* (ed. Y. Y. Renardy, A. V. Coward, D. Papageorgiou & S. M. Sun). SIAM.

Busse, F. H. 1981 On the aspect ratio of two-layer mantle convection. *Phys. Earth Planet. Inter.* **24**, 320–324.

Busse, F. H. & Sommermann, G. 1996 Double-layer convection: a brief review and some recent experimental results. In *Advances in Multi-Fluid Flows* (ed. Y. Y. Renardy, A. V. Coward, D. Papageorgiou & S. M. Sun). SIAM.

Cardin, Ph., Nataf, H.-C. & Dewost, Ph. 1991 Thermal coupling in layered convection: evidence for an interface viscosity control, from mechanical experiments and marginal stability analysis. *J. Phys. Paris* II **1**, 599–622.

Chandrasekhar, S. 1961 *Hydrodynamic and Hydromagnetic Stability*. Dover.

Cserepes, L. & Rabinowicz, M. 1985 Gravity and convection in a two-layered mantle. *Earth Planet. Sci. Lett.* **76**, 193–207.

Cserepes, L., Rabinowicz, M. & Rosemberg-Borot, C. 1988 Three-dimensional infinite Prandtl number convection in one and two layers with implications for the Earth's gravity field. *J. Geophys. Res.* **93**, 12009–12025.

Davaille, A. 1999*a* Two-layer thermal convection in miscible fluids. *J. Fluid Mech.* **379**, 223–253.

Davaille, A. 1999*b* Simultaneous generation of hotspots and superswells by convection in a heterogeneous planetary mantle. *Nature* **402**, 756–760.

Davaille, A., Girard, F. & Le Bars, M. 2002 How to anchor hot spots in a convecting mantle? *Earth Planet. Sci. Lett.* **203**, 621–634.

Davaille, A., Vidal, V., Le Bars, M. Jurine, D. & Carbonne, C. 2003 Imaging isotherms in viscous fluids. *Exps. Fluids* (in preparation).

Degen, M. M., Colovas, P. W. & Andereck, C. D. 1998 Time-dependent patterns in the two-layer Rayleigh-Bénard system. *Phys. Rev.* E **57**, 6647–6659.

Ellsworth, K. & Schubert, G. 1988 Numerical models of thermally and mechanically coupled two-layer convection of highly viscous fluids. *Geophys. J.* **93**, 347–363.

Herrick, D. L. & Parmentier, E. M. 1994 Episodic large-scale overturn of two-layer mantles in terrestrial planets. *J. Geophys. Res.* **99**, 2053–2062.

Howard, L. N. 1964 Convection at high Rayleigh number. In *Proc. 11th Intl Congr. Appl. Mech.* (ed. H. Görtler), pp. 1109–1115. Springer.

Krishnamurti, R. 1970 On the transition to turbulent convection. *J. Fluid Mech.* **42**, 295–320.

Le Bars, M. & Davaille, A. 2002 Stability of thermal convection in two superimposed miscible viscous fluids. *J. Fluid Mech.* **471**, 339–363.

Olson, P. 1984 An experimental approach to thermal convection in a two-layered mantle. *J. Geophys. Res.* **89**, 11293–11301.

Olson, P. & Kincaid, C. 1991 Experiments on the interaction of thermal convection and compositional layering at the base of the mantle. *J. Geophys. Res.* **96**, 4347–4354.

Olson, P. & Singer, H. 1985 Creeping plumes. *J. Fluid Mech.* **158**, 511–531.

Pellew, A. & Southwell, R. V. 1940 On maintained convective motion in a fluid heated from below. *Proc. R. Soc. Lond.* A **176**, 312–343.

Rasenat, S., Busse, F. H. & Rehberg, I. 1989 A theoretical and experimental study of double-layer convection. *J. Fluid Mech.* **199**, 519–540.

Renardy, Y. & Joseph, D. D. 1985 Oscillatory instability in a Bénard problem of two fluids. *Phys. Fluids* **28**, 788–793.

Renardy, M. & Renardy, Y. 1985 Perturbation analysis of steady and oscillatory onset in a Bénard problem with two similar liquids. *Phys. Fluids* **28**, 2699–2708.

Ribe, N. M. 1998 Spouting and planform selection in the Rayleigh-Taylor instability of miscible viscous fluids. *J. Fluid Mech.* **34**, 315–336.

Richter, F. M. & Johnson, C. E. 1974 Stability of a chemically layered mantle. *J. Geophys. Res.* **79**, 1635–1639.

Richter, F. M. & McKenzie, D. P. 1981 On some consequences and possible causes of layered convection. *J. Geophys. Res.* **86**, 6133–6142.

Sotin, C. & Parmentier, E. M. 1989 On the stability of a fluid layer containing a univariant phase transition: application to planetary interiors. *Phys. Earth Planet. Inter.* **55**, 10–25.

Sparrow, E. M., Goldstein, R. J. & Jonsson, V. K. 1964 Thermal instability in a horizontal fluid layer: effect of boundary conditions and non-linear temperature profile. *J. Fluid Mech.* **18**, 513–528.

Tackley, P. J. 2000 Mantle convection and plate tectonics: toward an integrated physical and chemical theory. *Science* **288**, 2002–2007.

Tait, S. & Jaupart, C. 1989 Compositional convection in viscous melts. *Nature* **338**, 571–574.

Turner, J. S. 1979 *Buoyancy Effects in Fluids*. Cambridge University Press.

Whitehead, J. A. & Luther, D. S. 1975 Dynamics of laboratory diapir and plume models. *J. Geophys. Res.* **80**, 705–717.